(E82-10166) HEAT FLUX ESTIMATES OVER VEGETATION DERIVED USING RADIOMETRIC SURFACE TEMPERATURES AND A BOUNDARY LAYER MODEL IN COMPARISON WITH SODAR-DERIVED VALUES M.S. Thesis (Pennsylvania State Univ.) 111 p

HC A06/MF A01

N82-22601

Unclas

G3/43 00166

The Pennsylvania State University
The Graduate School
Department of Meteorology

Heat Flux Estimates over Vegetation Derived Using Radiometric Surface Temperatures and a Boundary Layer Model in Comparison with Sodar-Derived Values

A Thesis in
Meteorology
by
James N. Cooper

Submitted in Partial Fulfillment
of the Requirements
for the Degree of

Master of Science

August 1981

James N. Cooper
James N. Cooper

We approve the thesis of James N. Cooper.

Date of Signature:	Signatories:
	Toby N. Carlson, Associate Professor of Meteorology, Thesis Advisor
15 June 1981	Dennis W. Thomson, Professor of Meteorology, Graduate Faculty Reader
June 22, 1981	Alfred K. Blackadar Alfred K. Blackadar, Professor and Head of the Department of Meteorology

ABSTRACT

An attempt is made to validate a method that uses radiometric surface temperatures and a boundary layer model to estimate surface energy budgets and characteristics. The surface temperatures are area-averaged values so the results from the Radiometric Data/Model System (RDMS) are also area-averages. Another remote sensing method, sodar, is used to obtain heat flux estimates on the same scale as the RDMS values for ground truth measurements. A simultaneous collection of radiometric surface temperatures from a hand-held radiometer and sodar data was made on seven days between mid-July and mid-October 1980. The comparison of the RDMS and sodar heat fluxes proved disappointing. Free convection conditions, required to produce sodar-derived heat fluxes, were inhibited by a terrain-induced low level inversion. Only three out of seven cases produced meaningful sodar heat fluxes. Of those three cases, one had good agreement and the other two had sodar heat fluxes 15 to 45 W m^{-2} lower than the RDMS values. Since the RDMS method is relatively untested, it was impossible to conclusively determine its validity from the results. There was evidence that the true heat flux was not underestimated by the RDMS, so it could be concluded that the Bowen ratios over well-watered vegetation were likely to be quite small.

TABLE OF CONTENTS

LIST OF TABLES

LIST OF FIGURES

LIST OF FIGURES (Continued)

LIST OF FIGURES (Continued)

ACKNOWLEDGEMENTS

I wish to thank Dr. Toby Carlson for his time and encouragement, Kenneth Underwood for teaching me whatever I wanted to know about the sodar, and each of my fellow graduate students who helped to collect the surface temperature data.

This research was supported by the National Aeronautics and Space Administration under grant NAS 5-24264 and by the Environmental Protection Agency under grant No. R805640-03

1.0 INTRODUCTION

1.1 DEVELOPMENT OF THE SATELLITE DATA/MODEL SYSTEM (SDMS)

Carlson and Boland (1978) developed a one-dimensional boundary layer model capable of predicting the surface temperature and the surface energy budget. They used the model to examine the relative importance of the various terrain parameters governing the response of the ground to heating. From a series of sensitivity tests, two parameters, the ground moisture availability and the ground conductance (thermal inertia), were found to dominate the response of the ground to solar radiation. Thus, they felt that if the values of moisture availability (M) and thermal inertia (P) for a surface could be obtained, initialization of the other variables in the model using standard meteorological data sources would produce ground temperatures accurate to ± 2C.

They noted that black body surface temperatures clearly showed the response of a given type of surface to heating. This result suggested a way of determining values of M and P for a surface. Carlson and Boland proposed to combine an inversion of the model output with a pair of observed radiometric surface temperatures. Surface temperature variations such as those measured by a satellite would be matched to the variations calculated by the model. From that matching, unique values of M and P for a surface would be defined. Given estimates of those two dominant parameters, the model could then calculate the heat flux and evaporation for the area observed by the satellite. Thus, Carlson and Boland felt that the substrate characteristics and surface energy budget for an area could be estimated from satellite observations combined with the output from a one-dimensional boundary layer model.

Augustine (1978) accelerated the linking of satellite data with the model by developing a technique to produce surface temperature maps for an area using radiometric satellite data. He produced day and night temperature maps of Los Angeles. Unfortunately, the satellite overpass times were just after sunrise and sunset, and the maps produced did not show the maximum diurnal temperature variation. The matching technique proposed by Carlson and Boland requires that surface temperatures be measured near the times of maximum and minimum heating. Thus, no attempt was made in Augustine's work to implement their procedure.

It was not until 26 April 1978 that a satellite capable of producing effective black body temperature measurements of the earth close to the times of maximum and minimum temperatures was launched. On that day, a small applications explorer satellite was launched by the National Aeronautics and Space Administration (NASA) as part of the Heat Capacity Mapping Mission (HDMM) The operational characteristics of the HCMM satellite are discussed by Barnes and Price (1980). By that time, the method for linking the one-dimensional boundary layer model with satellite-sensed surface temperatures had been perfected.

When HCMM data became available, the satellite data/model system was used to produce maps of M, P, heat flux, and evaporation for St. Louis and Los Angeles. Carlson et al. (1981) detailed the results of these cases. From the maps of M and P, they made conclusions concerning the mechanisms behind the urban temperature anomaly. The maps of heat flux and evaporation portrayed the spatial variation of the partitioning of solar radiation caused by differences in land use and vegetative cover.

Additional work was done using HCMM data by Kocin (1979) and DiCristofaro (1980). Kocin examined the patterns of M, P, heat flux and evaporation over a vegetated watershed in Missouri. He was able to relate specific regional features (forests, croplands, etc.) and rainfall to the analysis of moisture availability. Changes in the distribution of moisture availability were found to be co-dominated by rainfall amounts and changes in the surface's vegetative canopy. DiCristofaro produced maps of the ground characteristics and energy budget for both urban and rural areas. Variations in moisture availability and thermal inertia were shown to be responsible for the temperature differences between urban and rural regions. His results for the rural areas indicated that the variability in heat flux and evaporation was caused by variations in land use.

1.2 STATEMENT OF THE PROBLEM

Before employing the satellite data/model system (SDMS) for further investigations, the validity of its products needed to be established. Although the previously mentioned investigators have demonstrated the ability of the system to produce reasonable patterns of the surface energy budget and substrate characteristics, the values of these parameters needed confirmation by independent measurements.

Unfortunately, independent measurements of the same nature and type as the model products are not easily obtained. The estimates of all the parameters produced by the SDMS customarily use radiometric surface temperature measurements averaged over approximately 1 km^2. It follows that the values of moisture availability, thermal inertia, heat flux, and evaporation are also area-averaged. A large array of point measurements is usually required to determine area-averaged ground truth values for these parameters. However, the financial and physical resources for such a measurement program can be enormous. Thus, here we have used other methods in an attempt to verify the SDMS results.

One such method is aircraft measurements. DiCristofaro (1980) attempted to verify some of his results utilizing this procedure. He obtained aircraft measurements of surface heat and evaporative fluxes from the Sulfur Transport and Transformation in the Environment (STATE) project (Schiermeir et al., 1979). A comparison between results from the SDMS and the STATE data was attempted. Unfortunately, the results were inconclusive. The agreement was reasonable for the evaporative fluxes, but the aircraft measured values of heat flux were several times larger than the satellite derived values. It was noted, however, that the aircraft measured large heat fluxes in a forested area which displayed low daytime temperatures on the satellite pictures. In fact, the aircraft-measured heat fluxes for this area were only slightly lower than the values found in downtown St. Louis.

Another remote sensing method, sodar, can produce values of heat flux averaged over the same scale as the satellite measurements. The sodar measures the scattering of sound in a volume of air by temperature fluctuations. The scattering can be related to the temperature structure constant C_T^2. When free convection conditions exist in the atmosphere, the surface heat flux obeys a 4/3 power law between C_T^2 and height (Wyngaard et al., 1971). In this situation, the large C_T^2 values are concentrated in updrafts generated by the heating of the terrain and advected by the mean wind. Neff (1975) found regions of large C_T^2 that were localized at a horizontal scale of about 300m. Heat flux estimates derived from C_T^2 values during free convection conditions were therefore averaged over a section of the terrain upwind of the sodar antenna. The exact area of the average depended on the mean wind speed.

1.3 PURPOSE OF THE THESIS

A need existed to verify the values of the SDMS by independent measurement. One technique that can measure heat flux on the same scale as the SDMS is sodar. This research compared sodar measurements of heat flux with those from a version of the SDMS that used surface temperature measurements from a hand-held radiometer instead of a satellite. Radiometric temperature and sodar data were collected simultaneously on seven days in the summer and autumn of 1980 to provide the raw data for the two methods. The sodar data was processed by producing ten minute averages of C_T^2 profiles. If free convection conditions were present in the atmosphere, an estimate of the heat flux for that period could then be made from the profile. The heat flux estimates of the modified SDMS and the sodar were analyzed over the diurnal cycle. An effort was made to determine the validity of the modified SDMS values by comparing them with the sodar results.

2.0 METHODS OF ESTIMATING THE HEAT FLUX

2.1 THE SATELLITE DATA/MODEL SYSTEM (SDMS) METHOD

The one-dimensional boundary layer model used and the procedure of linking the model with the satellite data in the SDMS have been well documented (see Carlson and Boland (1978), Carlson et al. (1981), Dodd (1979), Kocin (1979), and DiCristofaro (1980)). Thus, only a brief summary of the SDMS is presented here.

The purpose of the SDMS is to produce maps of substrate characteristics and surface fluxes for an area using surface temperature measurements near the maximum and minimum of the heating cycle. The maps are created by matching the observed surface temperatures to surface temperatures calculated for the observation time by the model. The basic assumption which allows the transformation between surface temperatures and substrate parameters to be made is that a given model maximum/minimum temperature pair is computed from a unique pair of M and P values and vice-versa. Thus, a measured temperature pair can be combined with the model output to infer specific values of M and P. Carlson and Boland (1978) found that M and P are the dominant factors in determining the partitioning of incoming solar radiation into sensible and latent heat flux at the surface. Accordingly, solutions yielding a unique M and P also correspond to a unique solution of the surface energy budget. The model output at the time of the temperature measurements for a wide range of M and P values is represented by a set of regression equations involving the maximum/minimum temperature pairs as predictors. In this manner, substrate characteristics and the surface energy budget are obtained when an observed maximum/minimum temperature pair is inserted into the regression equations. Maximum/minimum surface temperature maps from an aircraft or satellite can be transformed using the regression equations into maps of the two surface parameters and the surface fluxes.

2.2 SODAR HEAT FLUX THEORY

A monostatic sodar measures acoustic energy backscattered by the atmosphere. This energy can be related to a temperature structure parameter C_T^2 which, in turn, can be used to estimate heat flux.

The radar equation for backscattered energy can be modified to apply to a monostatic sodar. Following Underwood (1981), a form of the monostatic sodar equation is

$$P(r) = P_o \frac{A_r}{r^2} L_v e^{-2\overline{\alpha}r} E \, \sigma(\pi) \tag{2.1}$$

where

$P(r)$ = received acoustic power,

P_o = transmitted acoustic power,

A_r = cross-sectional area of the antenna,

r = range of scatterer from antenna,

$\overline{\alpha}$ = path averaged molecular attenuation coefficient,

L_v = length of the scattering pulse in space,

E = turbulence induced excess attenuation,

$\sigma(\pi)$ = backscattering cross section.

The backscattering cross section σ is the fraction of the incident power backscattered per unit solid angle. With proper calibration of the sodar system and estimates of the attenuation, Equation 2.1 can be used to obtain values of σ. Those values are the basis for estimating heat flux with the sodar. However, the calculation is done indirectly through another variable, the temperature structure parameter C_T^2, which is related to both σ and heat flux.

C_T^2 is defined as

$$C_T^2 = \overline{[T(x) - T(x+r)]}/r^{2/3} \tag{2.2}$$

where C_T^2 represents the variance of the temperature difference between two points a distance r apart and r is assumed to be in the inertial subrange. Using Tatarski (1971) it can be shown that σ is related to C_T^2 in this fashion:

$$\sigma = 0.0039\ k^{1/3}\ C_T^2/T^2 \quad . \tag{2.3}$$

Wyngaard et al. (1971) derived the free convection limit

$$C_T^2 = \frac{3}{4}\left(\frac{\overline{T}}{kg}\right)^{2/3}\left(\frac{H_o}{\rho C_p}\right)^{4/3} z^{-4/3} \tag{2.4}$$

where

k = the von Karman constant,

$\overline{T}$ = the average air temperature,

g = gravity,

ρ = density,

C_p = the specific heat at constant pressure,

H_o = the heat flux.

Coulter and Wesely (1980) added a humidity correction factor γ_{so} to equation 2.4 where

$$\gamma_{so} = \{[1 + (0.07/\beta)^2]/[1 + (0.06/\beta)^2]\}^{3/4} \times (1 + 0.07/\beta_s)^{-1} \quad . \qquad (2.5)$$

Thus, when free convection conditions exist, sodar, by measuring σ, can be used to estimate the heat flux.

3.0 DATA COLLECTION

3.1 DESCRIPTION OF FIELD EXPERIMENT

The SDMS requires measurements of the surface temperature near the maximum and minimum of the heating cycle to produce estimates of heat flux. The SDMS was designed to utilize temperature data from polar orbiting satellites that pass over a site at the proper points in the heating cycle. The surface temperatures from these satellites represent an average value for an area of one pixel, which is about one half to one square kilometer for the highest resolution infrared satellite radiometers. SDMS values of heat flux were intended originally to be calculated from satellite data. Unfortunately, no satellite capable of producing surface temperature measurements at the optimum times was operational during the period of the experiment. Thus, it was necessary to simulate satellite measurements by conducting a small field experiment to collect the temperature data required to calculate the SDMS heat flux values. The necessary surface temperature values near the maximum and minimum of the heating cycle were recorded using a hand-held radiometer in an observation technique, to be described below, which was designed to determine an area-averaged temperature value. This modified version of the SDMS was called the Radiometric Data/Model System (RDMS). The acoustic signal returns of the sodar were collected at the same time and stored on magnetic tape to later be converted into heat fluxes.

The locale for the field experiment was the Rock Springs Agricultural Research Center of The Pennsylvania State University.

This facility is situated several miles from the Penn State campus (see Figure 3.1) and was chosen because it is the site of the Meteorology Department's sodar antenna. The area surrounding the sodar consists mainly of heterogeneous cropland, in which large fields of alfalfa, corn, and soybeans plus small test plots of alfalfa, corn, and oats are present within 500m of the antenna. A picture of the Rock Springs site is presented in Figure 3.2.

The duration of the experiment was July to October 1980. Since the boundary layer model employed in the RDMS procedure can simulate only clear sky and non-advective conditions, the temperature and sodar data were collected only when those conditions were present. In all, seven days met the criteria for data collection as demonstrated by the strong diurnal variation in the air temperature traces recorded at Penn State for each case (see Figures 3.3-3.9). A summary of the dates and weather conditions of each data collection day is presented in Table 3.1.

3.2 SURFACE TEMPERATURE DATA COLLECTION

The radiometer used in this research was a Barnes PRT-5 on loan from the Environmental Protection Agency (EPA). The radiometer was calibrated at Penn State by using a calibration box where the radiometer views a 'black box' cavity with a water bath of variable known temperature. The temperature reading of the radiometer is compared with the water temperature. It was discovered through this process that the radiometer consistently gave readings 1.5 to 2.0C too warm. Thus, all temperature readings from the field were corrected before final use by subtracting 1.7C from the raw value.

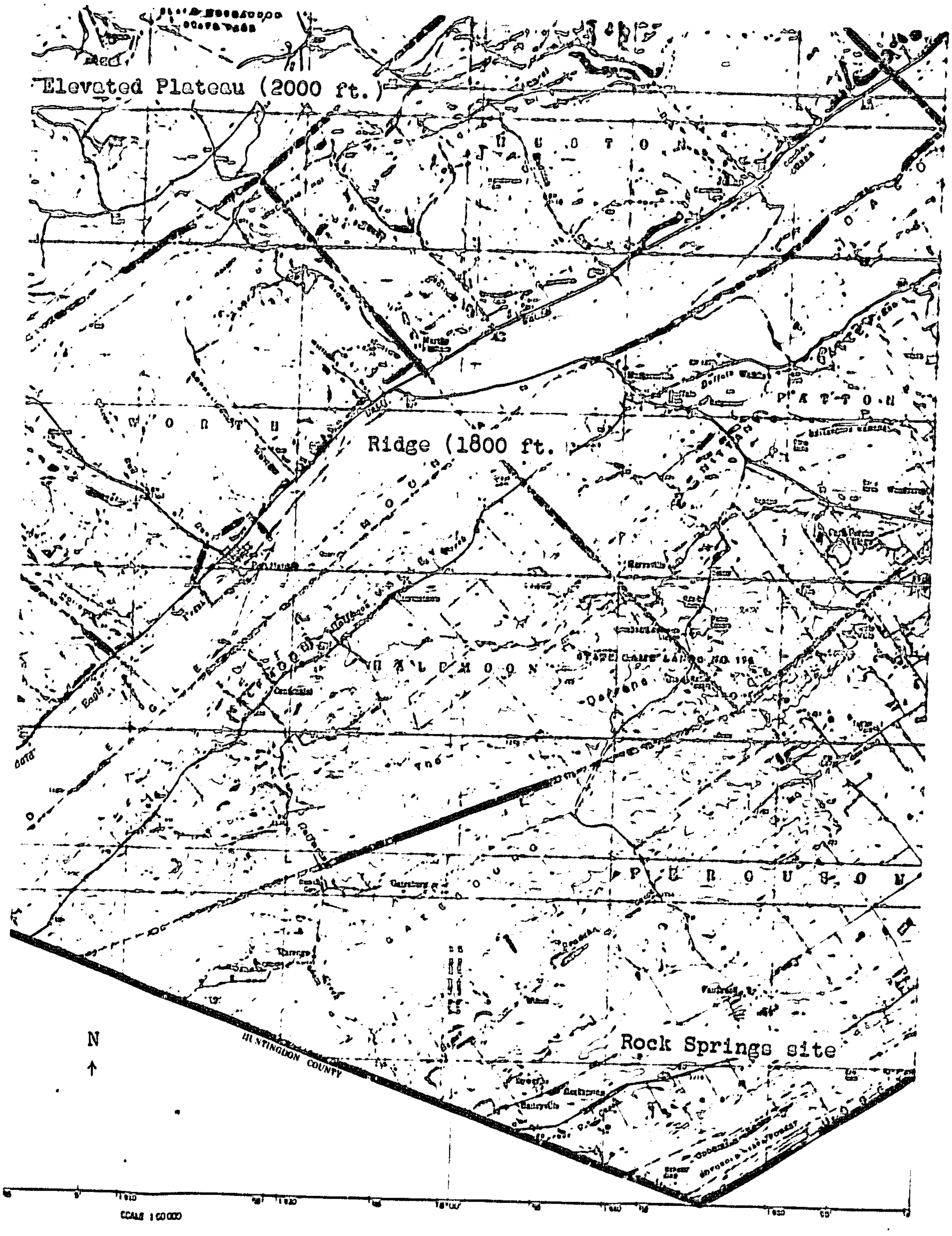

Figure 3.1 A map showing the location of the Rock Springs site. (Source: U.S. Geologic Survey Map NK1810, stock number V501 x NK1810).

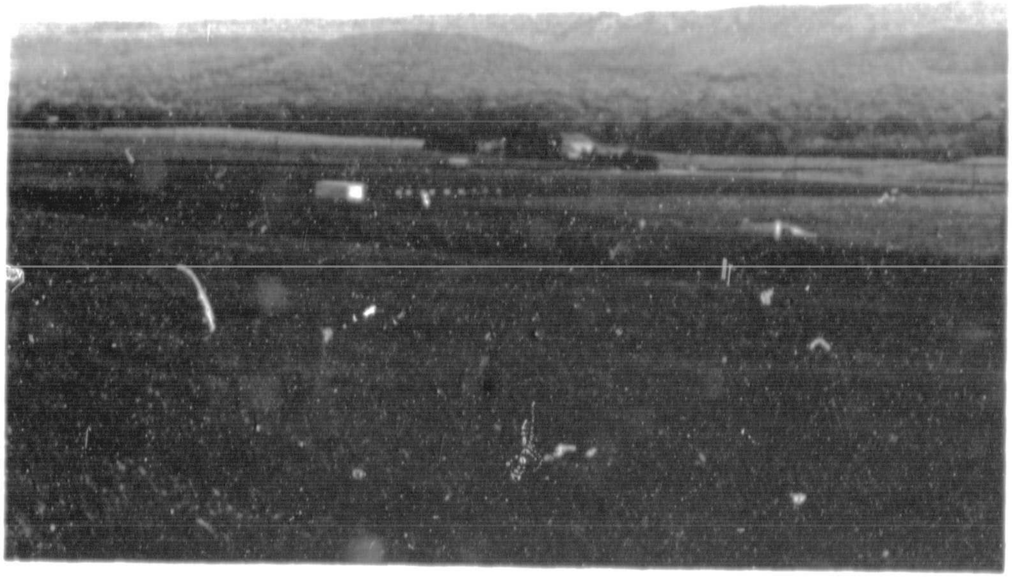

Figure 3.2 A section of the Rock Springs Agricultural Research Center of The Pennsylvania State University where the sodar and surface temperature data for this experiment were collected.

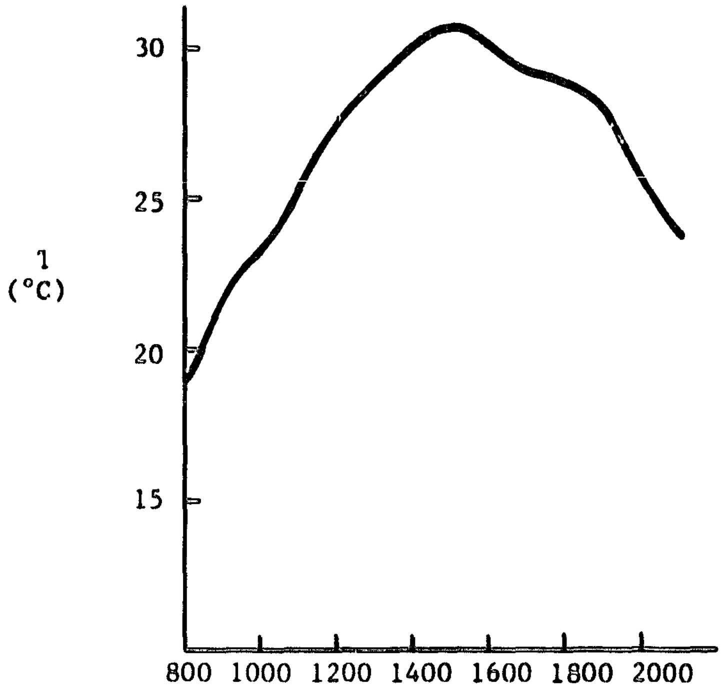

Time (EST)

Figure 3.3 Air temperature record for Case 1.

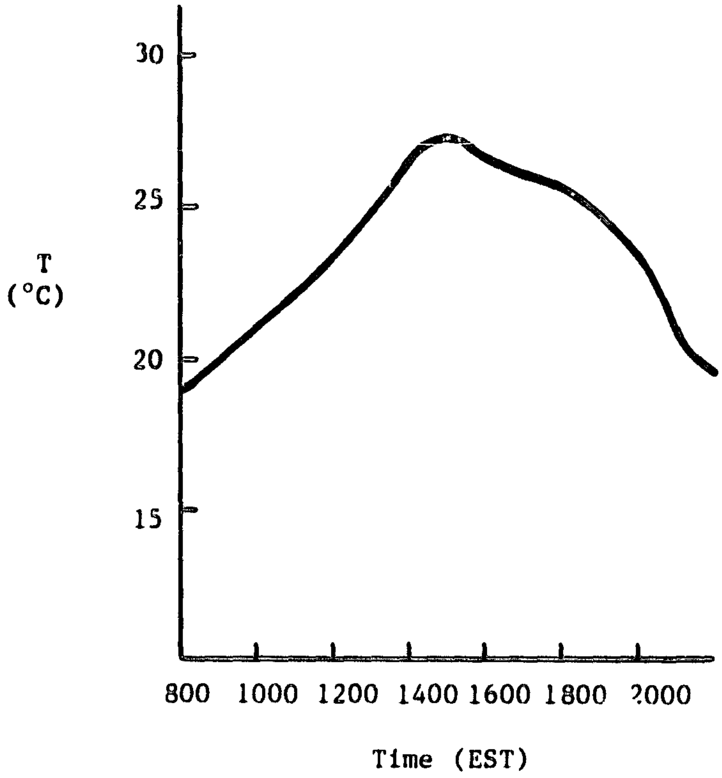

Figure 3.4 Air temperature record for Case 2.

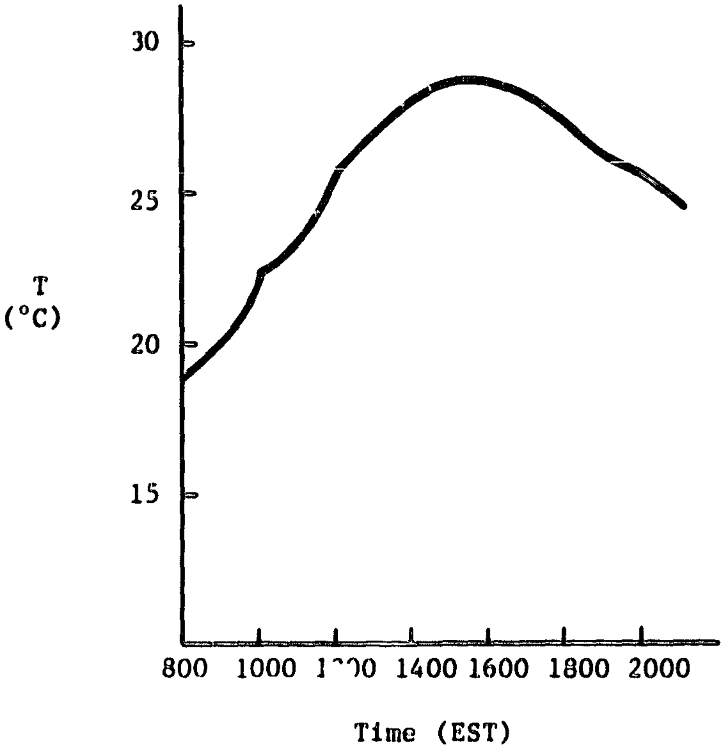

Figure 3.5 Air temperature record for Case 3.

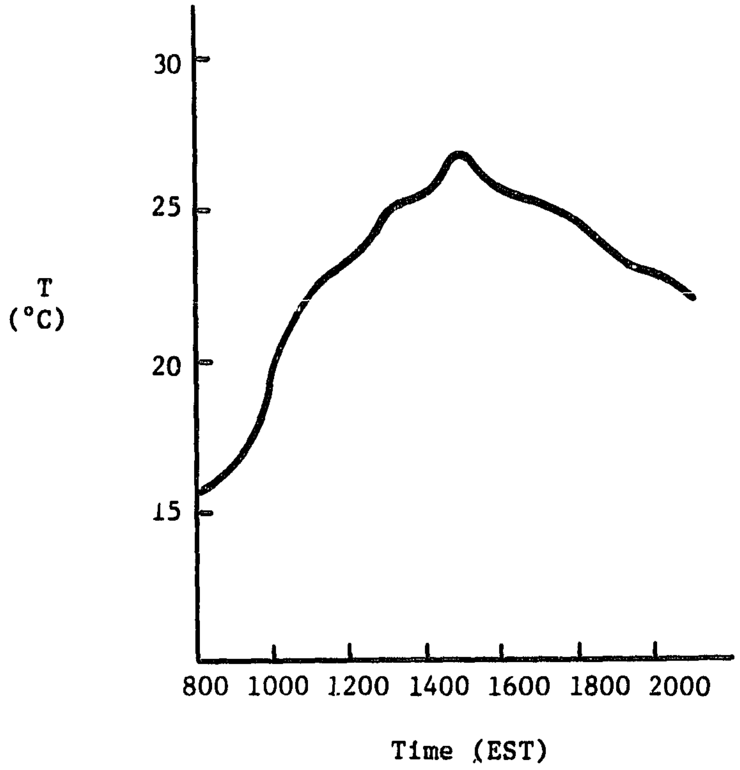

Figure 3.6 Air temperature record for Case 4.

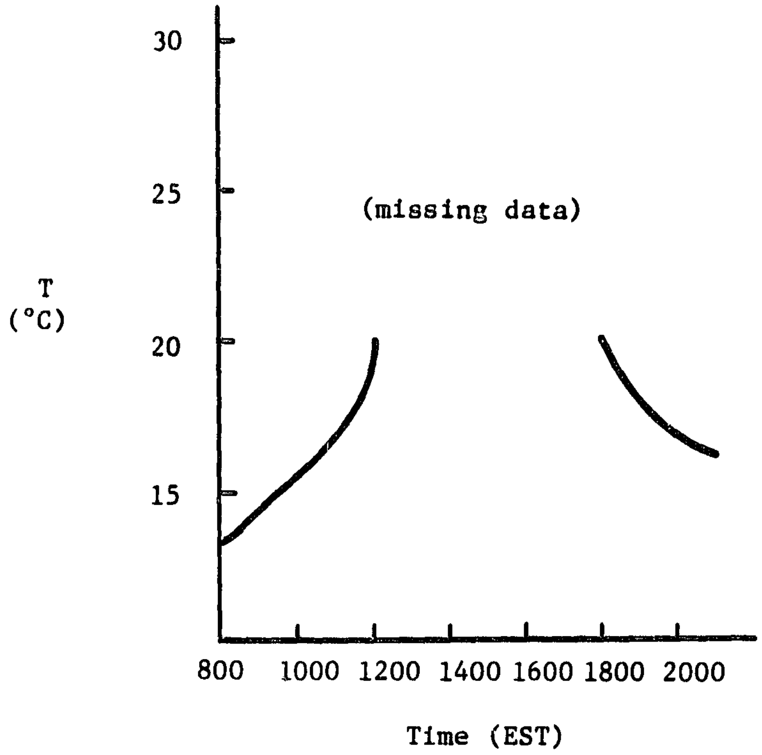

Figure 3.7 Air temperature record for Case 5.

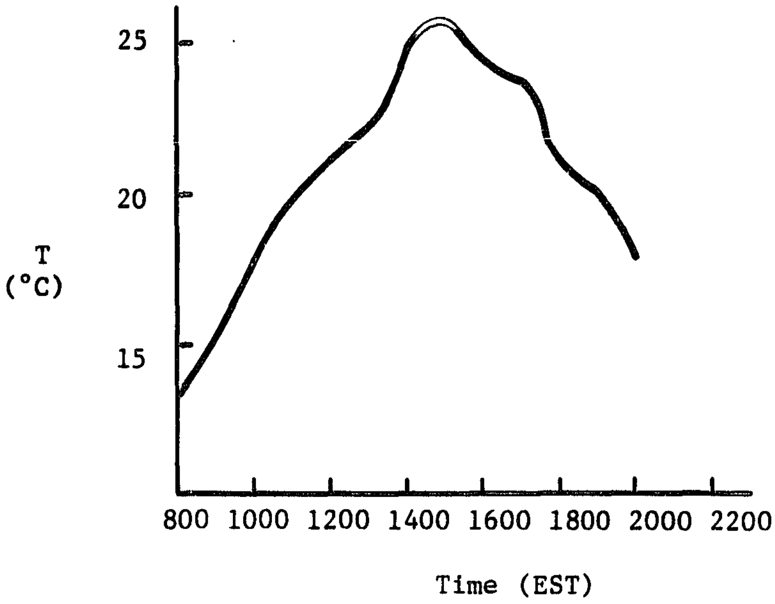

Figure 3.8 Air temperature record for Case 6.

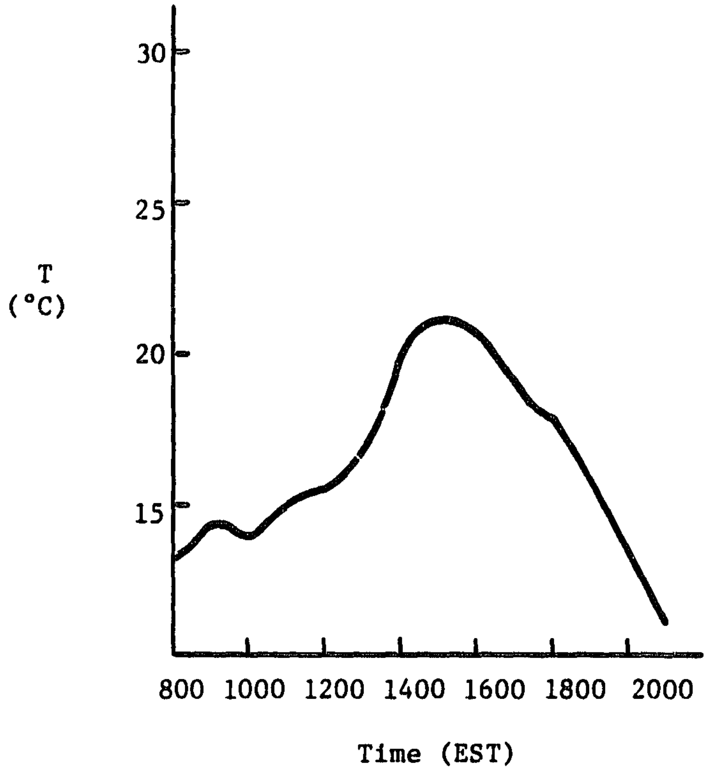

Figure 3.9 Air temperature record for Case 7.

Table 3.1 Summary of dates and conditions of data collection days.

Case	Date	Air Temperature (C)	Remarks
1	July 11	30	High thin cirrus, mostly south. Very thin, cover $\sim$ 0.5 of sky.
2	July 24	28	Some cumulus, $\sim$ 0.2 of sky. Wind NNE, light-breezy.
3	July 25	30	Hazy, Mt. St. Helens volcanic ash? Few small cumulus, < 0.1 of sky.
4	September 10	20	Winds breezy, N 0.1-0.2 cumulus clouds, sun mostly out.
5	September 11	24	Perfectly clear, some wind.
6	September 19	21	Winds light, NW Clear, < 0.1 sky cover, few cirrus.
7	October 9		Clear with a good view. Very scattered clouds, very turbulent.

The idea of using a hand-held radiometer (also called an infrared thermometer) to make surface temperature measurements of vegetation has been exploited previously on numerous occasions. Fuchs and Tanner (1966) found that, given the emissivity of the surface and the reflected atmospheric radiation, they could measure vegetative canopy temperatures with a radiometer to ± 0.1C.

Fuchs et al. (1967) measured crop surface temperatures using a radiometer. They examined the dependence of the temperature on viewing angle and solar azimuth angle (see Figure 3.10).

The incident angle had a minor effect on the measured temperature with variations usually less than 1C. Lower temperatures were recorded for incident angles near normal and greater than 60 degrees. At the small viewing angles, the radiometer looks deeply into the vegetation and sees more of the shaded (cooler) portions of the vegetation and ground surface. At large incident angles, the radiometer sees plant tips plus the horizon and therefore can produce a lower reading.

The solar azimuth angles had an effect in the case of Fuchs et al. (1967) only when the radiometer was viewing row crops. In this case, when the radiometer was facing the sun and the crop rows formed an angle greater than 10 degrees with the sun, temperatures were consistently 1.3C lower than when the radiometer viewed the same crops while pointed away from the sun. This difference was confirmed by leaf temperature measurements made with thermocouples. The radiometer views primarily shaded leaves at a solar azimuth angle of 0 degrees, versus the primarily sunlit leaves when the solar azimuth angle of the radiometer is 180 degrees. Fuchs et al. also found a

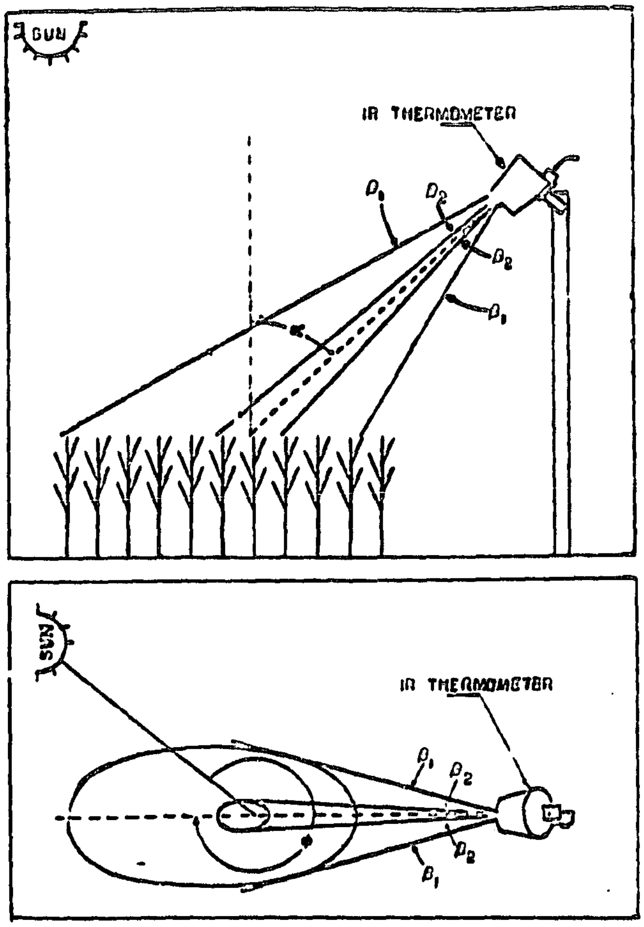

Figure 3.10 Schematic of the incident angle α, and the solar azimuth angle ϕ of the radiometer sensing beam. The field of view of wide and narrow beam instruments is given by β_1 and β_2, respectively. (Source: Fuchs et al., (1967)).

± .3C variation in time when the viewing angle was kept constant. They felt this variation was caused by air turbulence changing the ventilation of the crop leaves. A 30 degree field of view radiometer produced less variation in temperature measurements than a 7 degree field of view instrument since it averaged the temperature over a larger area.

The observation technique for the radiometric surface temperatures in the Rock Springs data collection was designed to enable one temperature to be determined for the entire site. A hand-held radiometer with a narrow field of view can only scan a small area. Thus, to produce an average value for the site, the observation technique had to satisfy two objectives:

1. Maximize the area that the radiometer viewed in one scan.
2. Provide a large number of temperature readings to obtain temperature values of all the crops present at the site.

The first step in maximizing the area viewed by the radiometer was to use a wide angle field of view lens. Further, the radiometer was operated at a height of about 5m above the surface from a site atop a tower mounted on a mobile van (see Figure 3.11). Finally, temperature measurements were made at three or more locations by driving the van/tower platform around the site.

Twelve temperature observations were made at each site. Because of the surface temperature variations with incident angle and solar azimuth angle noted by Fuchs et al. (1967), the observations were made at three incident angles at each of four solar azimuth angles (see Figure 3.12). The temperature values were recorded both manually

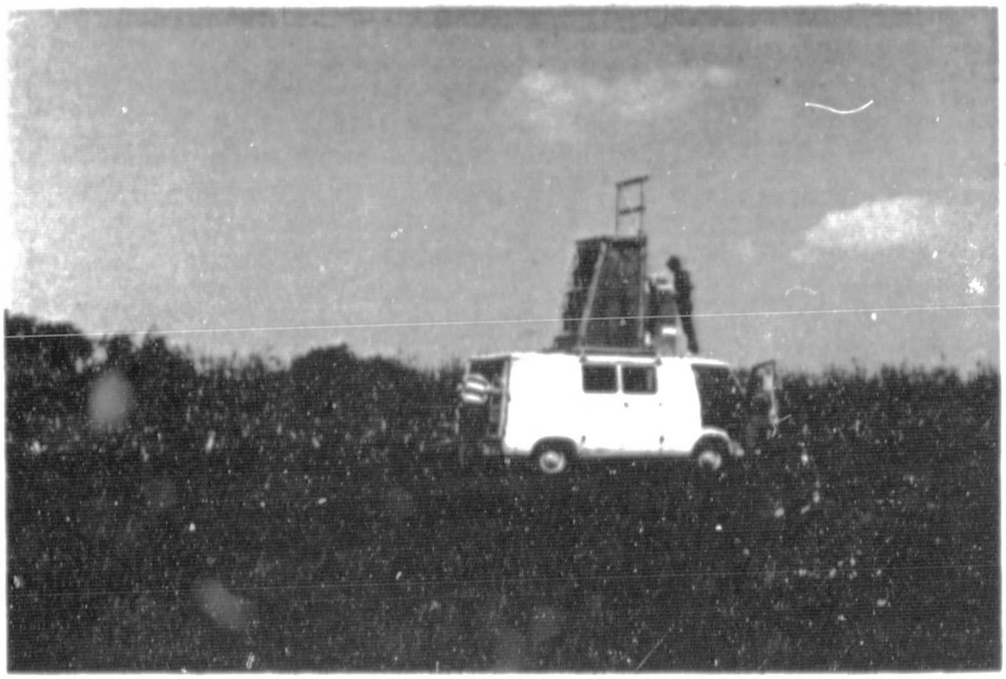

Figure 3.11 Van/tower platform that surface temperature measurements were made from using a hand-held radiometer.

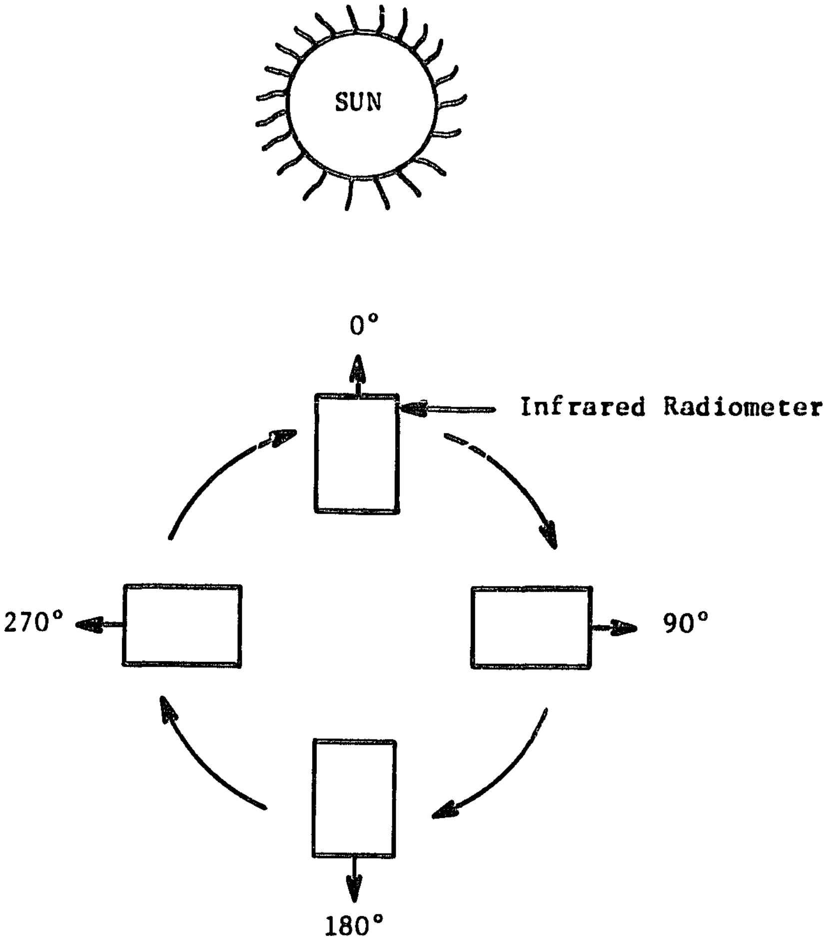

Figure 3.12a The four solar azimuth angles at which surface temperature data were measured.

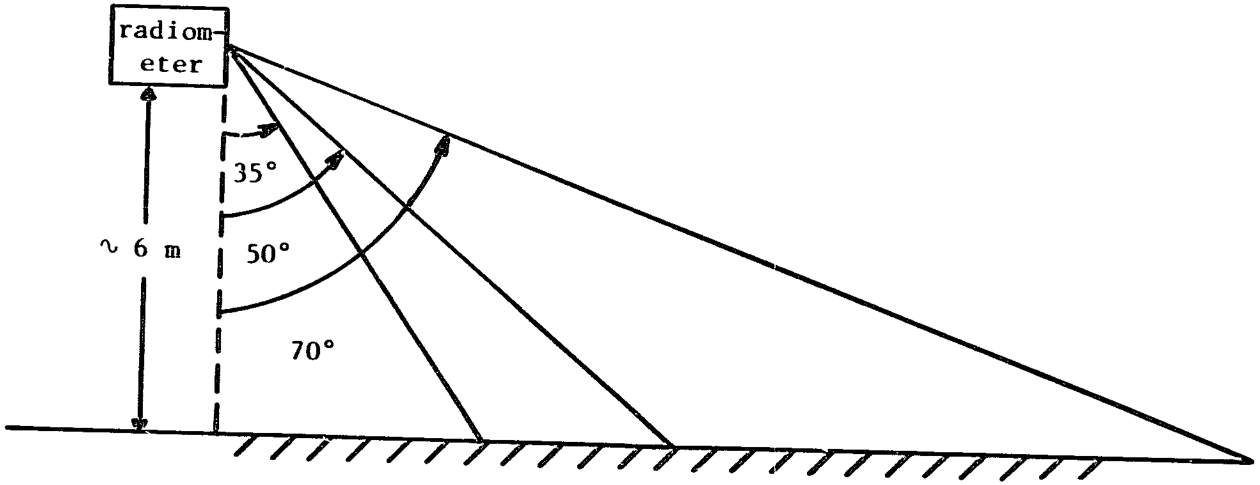

Figure 3.12b Incident angles of the radiometer used to take three surface temperature measurements at each solar azimuth angle.

and automatically by means of a strip chart recorder. Additionally, the type of vegetation viewed by the radiometer for each observation was noted, as were the local weather conditions (see Table 3.1).

Unlike Fuchs and Tanner (1966), in this field experiment the vegetative emissivity was assumed to be equal to one, although plant canopies typically have an emissivity of about .97. Therefore, the amount of atmospheric downwelling longwave radiation reflected by the vegetation was not calculated. The high degree of accuracy that Fuchs and Tanner achieved with their radiometric temperature measurements was not required for this experiment. A detailed discussion of the error produced by assuming a vegetative emissivity of one is given in Appendix A. The results show that the temperatures measured in this experiment are accurate to ± 0.5C.

Thus, the result of the radiometer part of the data collection was 36 surface temperatures measured over a variety of vegetation types. Temperature observations were made twice on a data collection day; first at approximately 1200 EST and again just after 0000 EST the following night.

3.3 SODAR DATA COLLECTION

The sodar used in the Rock Springs data collection was a modified Aerovironment Model 300. The sodar was calibrated on June 11, 1980, using the method described by Underwood (1978). No post-experiment calibration was performed.

The received acoustic energy of the Aerovironment is usually qualitatively recorded on a facsimile display. At Penn State, however, the system has been modified to allow the received signal to be both quantitatively displayed in false color imagery and logged on magnetic tape.

Figure 3.13 is a block diagram of the sodar system used in this experiment. The Data General Nova 2/10 minicomputer triggers a burst of 1600 hz acoustic energy from the Aerovironment every eight seconds. After a pause of .3 ms, the sodar becomes a receiver and converts the backscattered acoustic energy into a voltage. The voltage signal is transformed in a coupler for transmission via phone line from the site back to the computer laboratory. There a demodulator converts the signal back to a voltage that is sampled at 50 hz by an analog to digital converter. The Nova 2/10 processes the digitized signal, displaying it in false color on a video terminal and storing it on magnetic tape.

This entire process is automated. On the morning of a data collection day, the data logging program was entered into the minicomputer and the phone link with Rock Springs established. Then the sodar data was logged until the evening of that day at which point the data collection program was terminated by the user.

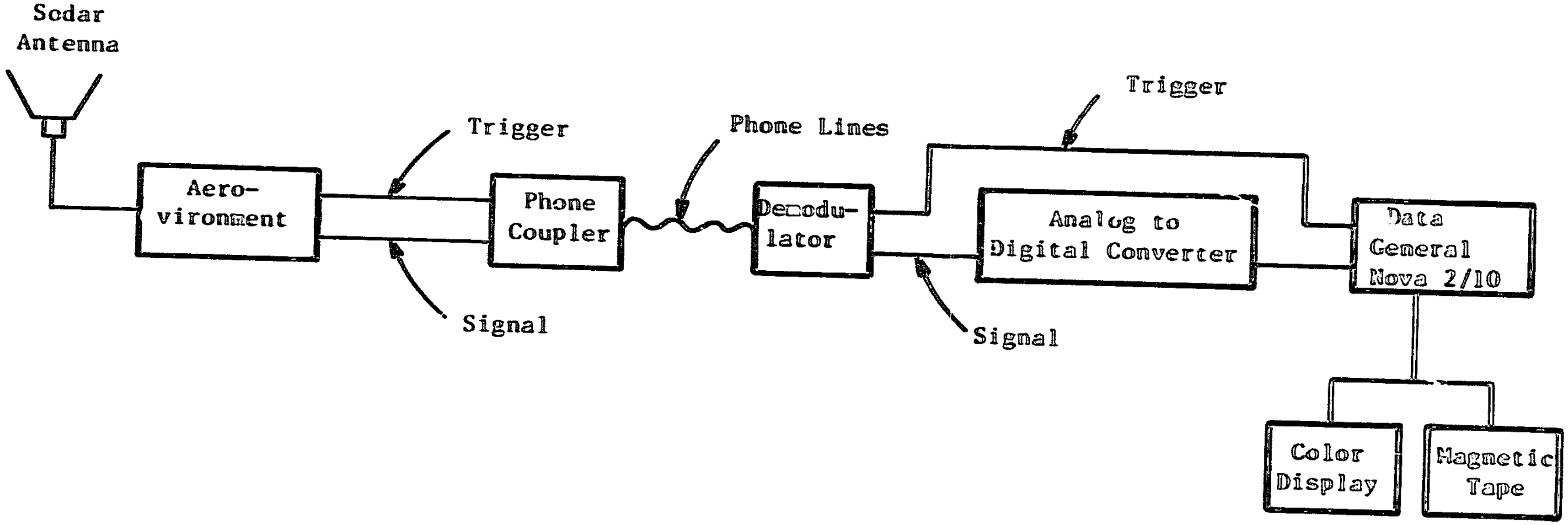

Figure 3.13 Block diagram of the system used to collect the sodar data in this experiment.

4.0 DATA ANALYSIS

4.1 INTRODUCTION

After the last data collection day on October 19, 1980, the process of converting the raw sodar and temperature data into heat fluxes began. The temperatures were analyzed to produce a single day/night pair of surface temperatures for each case. The temperature pair was then used in the RDMS to determine the heat flux for that case. The sodar data was plotted and examined for periods when free convection conditions were present. During those periods, heat fluxes were estimated with the sodar.

4.2 SURFACE TEMPERATURE DATA

The temperature data collection process yielded 36 day and night temperature values for each case. Figures 4.2-4.8 display the raw temperature data for each case and the symbols are explained in Figure 4.1. Note the large amount of variation present. The average difference for the seven cases between the high and low daytime values is 10C. Highlighted in Figures 4.2-4.8 are the three main causes of this variation:

1. The viewing angle of the radiometer.
2. The solar azimuth angle of the radiometer.
3. The type of crop viewed by the radiometer.

A further discussion of each of these factors follows.

Fuchs et al. (1967) showed that when using a 30 degree field of view lens, extreme incident angles (> 60 degrees) tend to produce

DAY TEMPERATURES

Solar Azimuth Angle

		0°	90°	180°	270°
Incident Angle	70°	•	|	Δ	/
	50°	• •	| |	ΔΔ	//
	35°	• • •	| | |	ΔΔΔ	///

NIGHT TEMPERATURES

Incident Angle	70°	+
	50°	/
	35°	Δ

Vertical lines inside a box indicate two or more measurements of that value were obtained.

CROP ABBREVIATIONS

C = Corn
A = Alfalfa
G = Grass
S = Soybeans

SHADED BARS

The shaded bars represent the best estimate of two standard deviations around the area-averaged temperature determined from the data.

Figure 4.1 Explanation of the symbols used in the radiometric surface temperature charts (Figures 4.2-4.8).

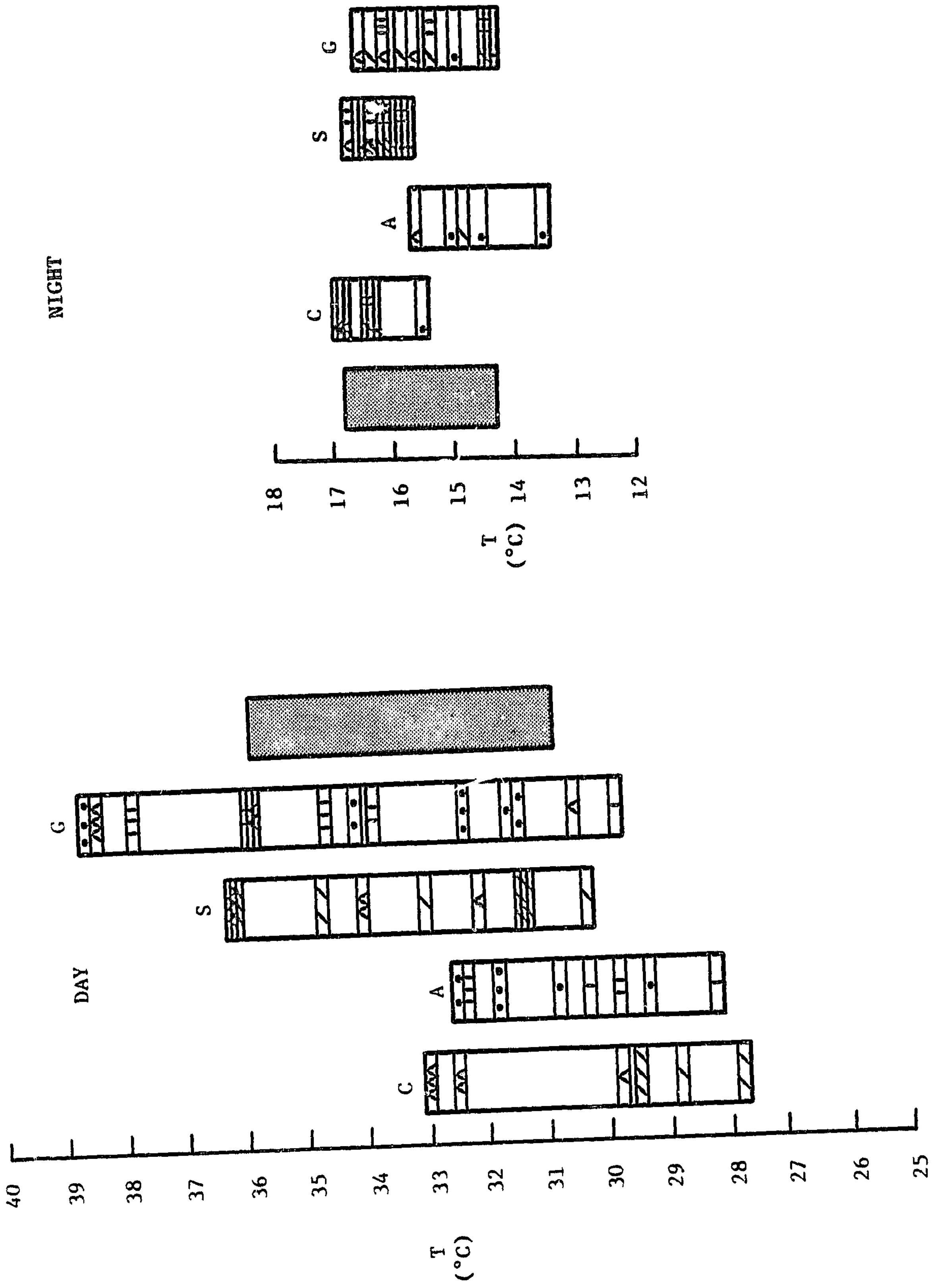
NIGHT
C
A
S
G
18
17
16
15
14
13
12
T
(°C)
DAY
C
A
S
G
40
39
38
37
36
35
34
33
32
31
30
29
28
27
26
25
T
(°C)

PRECEDING PAGE BLANK NOT FILMED

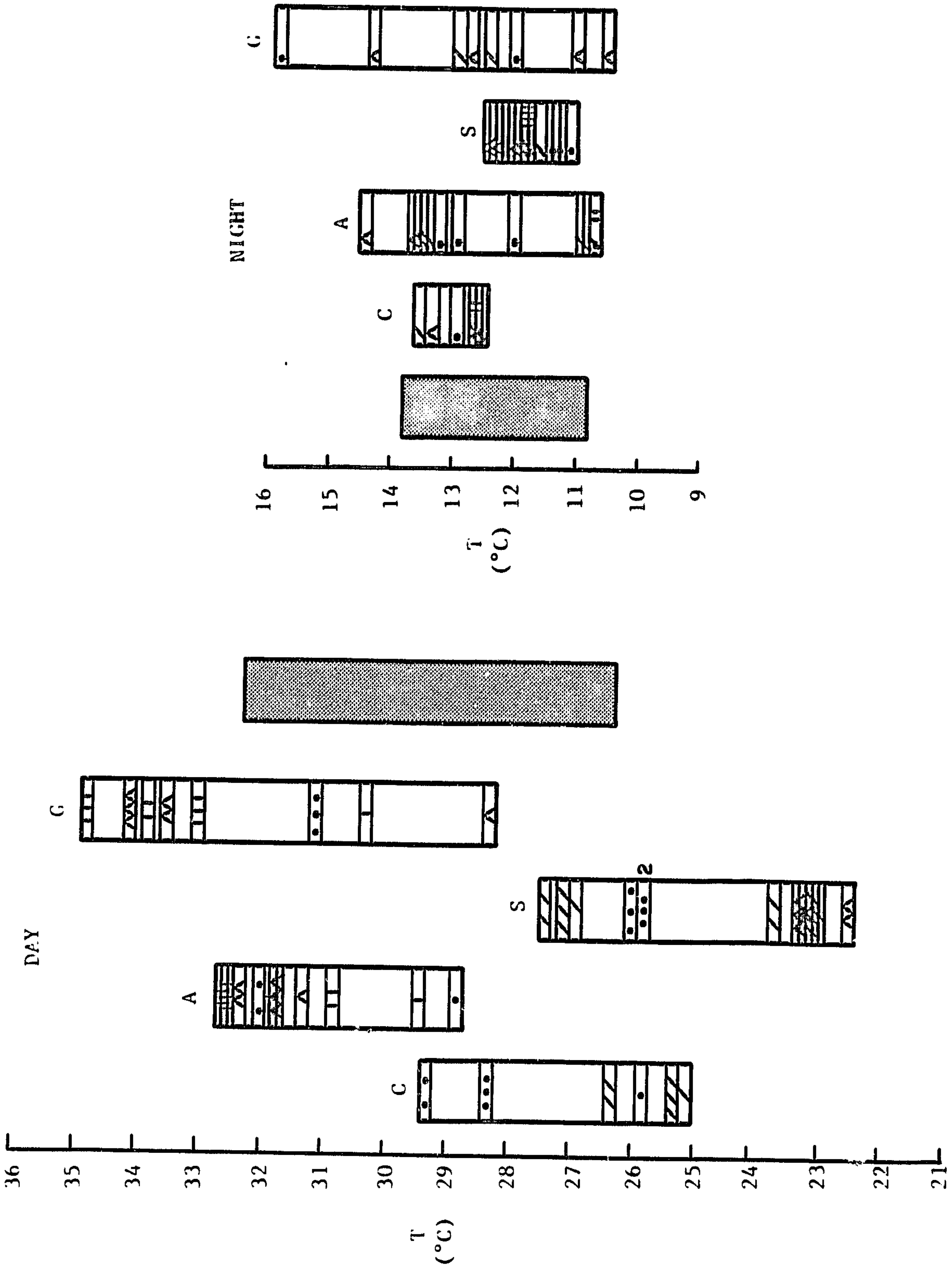

Figure 4.4 Radiometric surface temperature measurements for Case 3 (July 25). See Figure 4.1 for an explanation of the symbols.

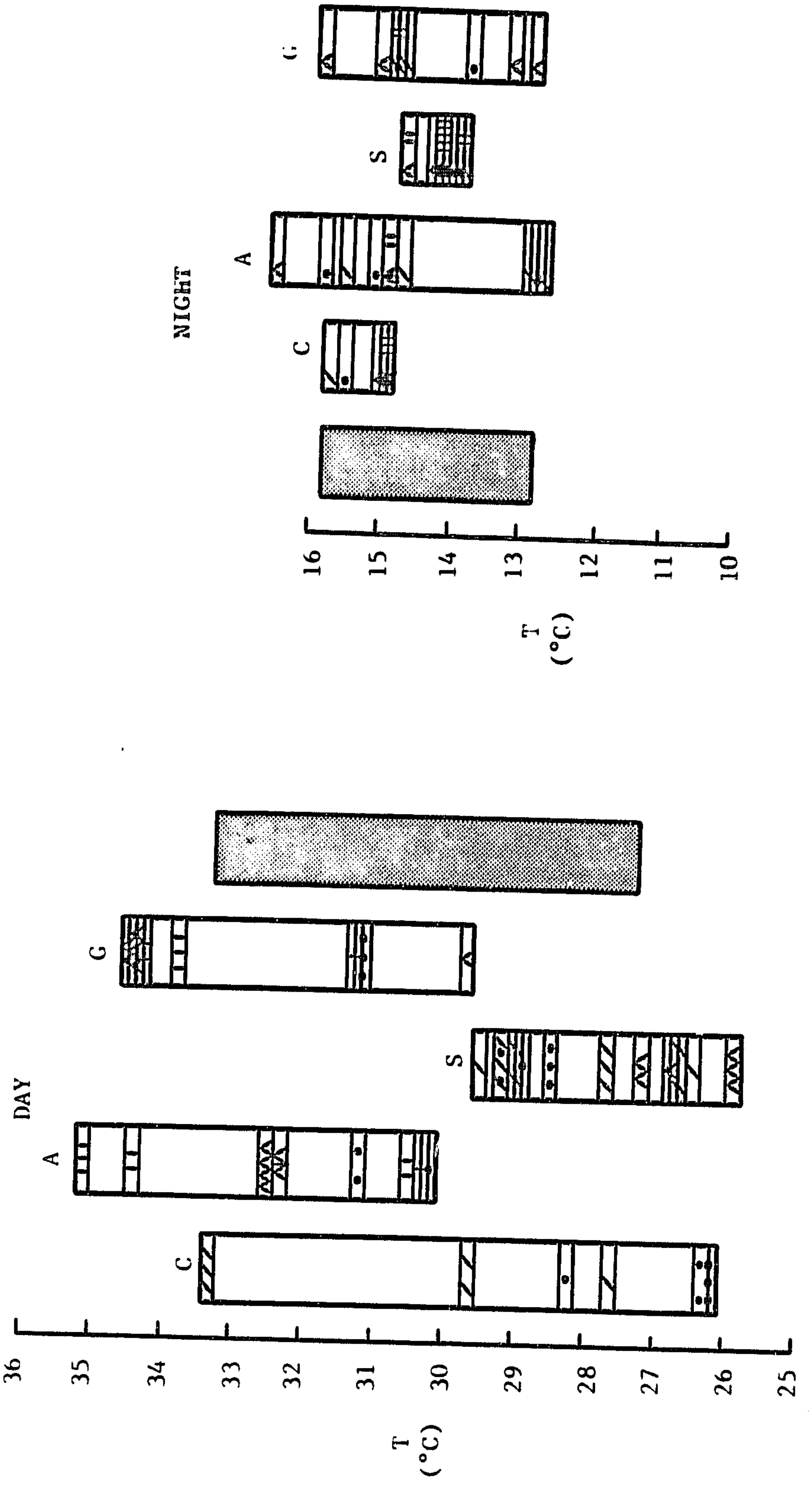
DAY
C
A
S
G
T
(°C)
36
35
34
33
32
31
30
29
28
27
26
25
NIGHT
C
A
S
G
T
(°C)
16
15
14
13
12
11
10

Figure 4.5 Radiometric surface temperature measurements for Case 4. For an explanation of the symbols see Figure 4.1.

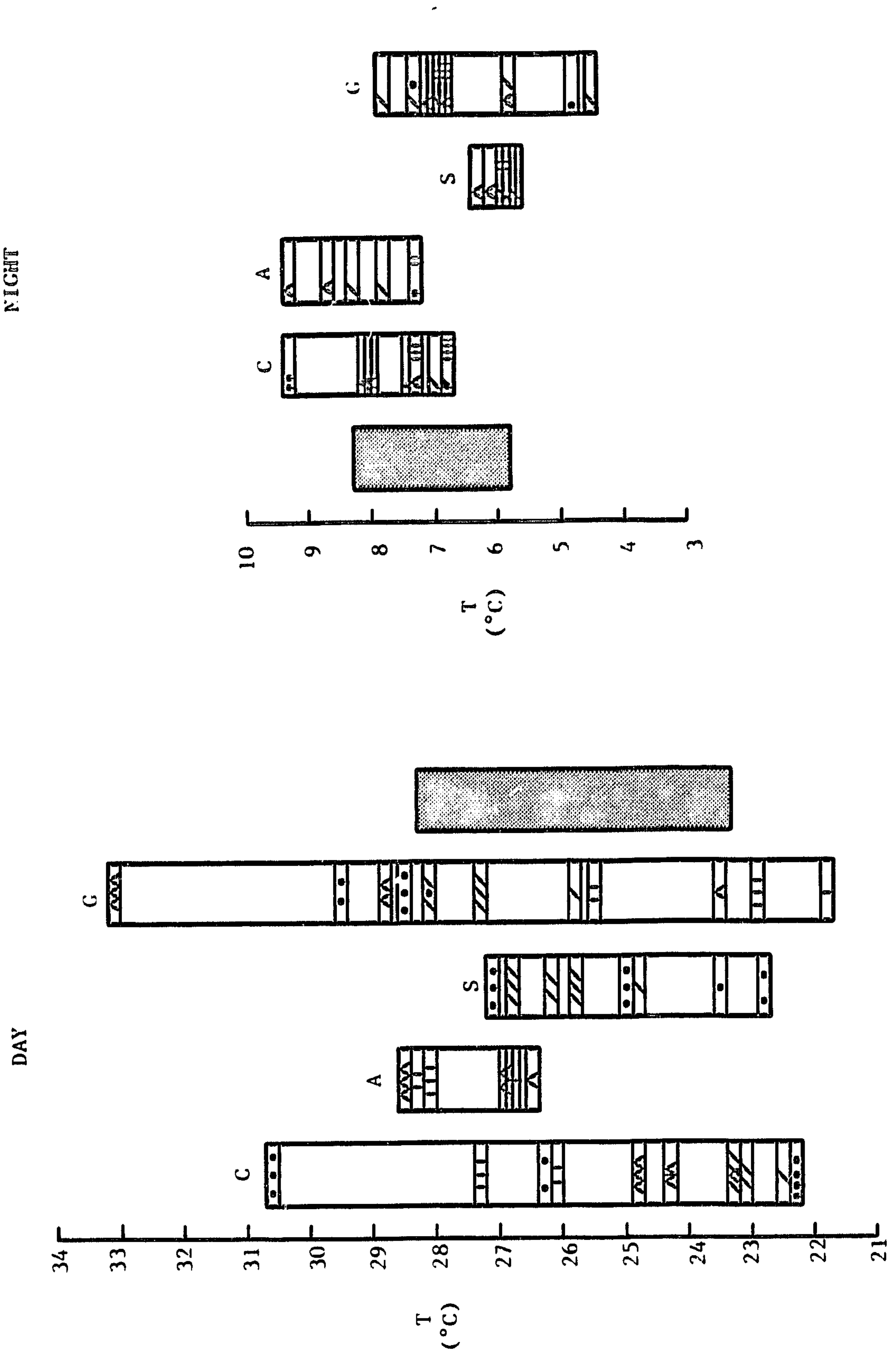
NIGHT
C
A
S
G
10
9
8
7
6
5
4
3
T
(°C)
DAY
C
A
S
G
34
33
32
31
30
29
28
27
26
25
24
23
22
21
T
(°C)

Figure 4.6 Radiometric surface temperature measurements for Case 5 (day only). For an explanation of the symbols see Figure 4.1.

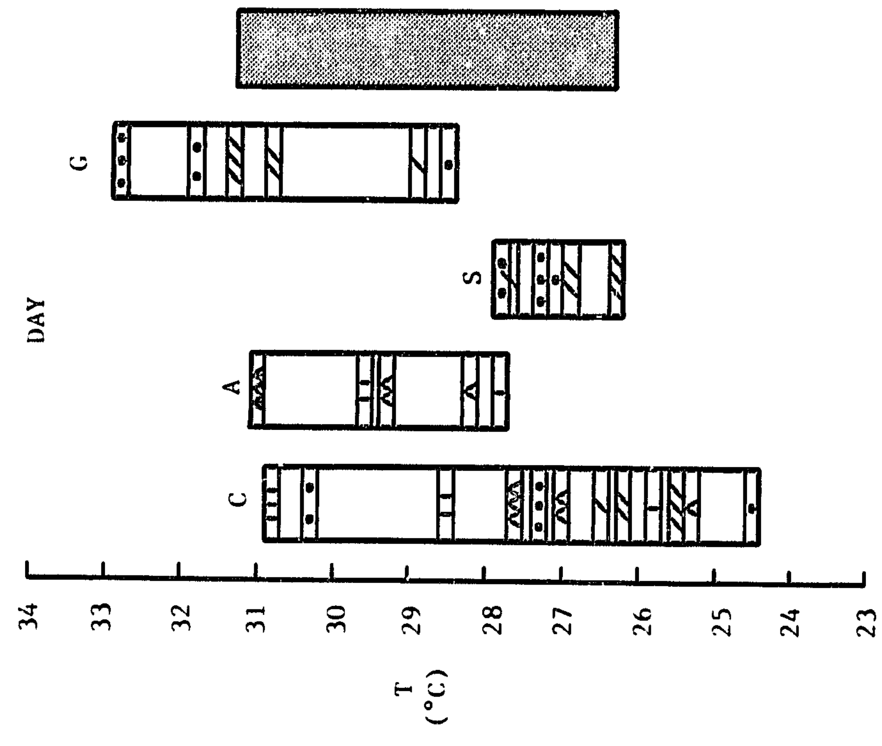
DAY
C
A
S
G
T (°C)
34
33
32
31
30
29
28
27
26
25
24
23

Figure 4.7 Radiometric surface temperature measurements for Case 6. For an explanation of the symbols see Figure 4.1.

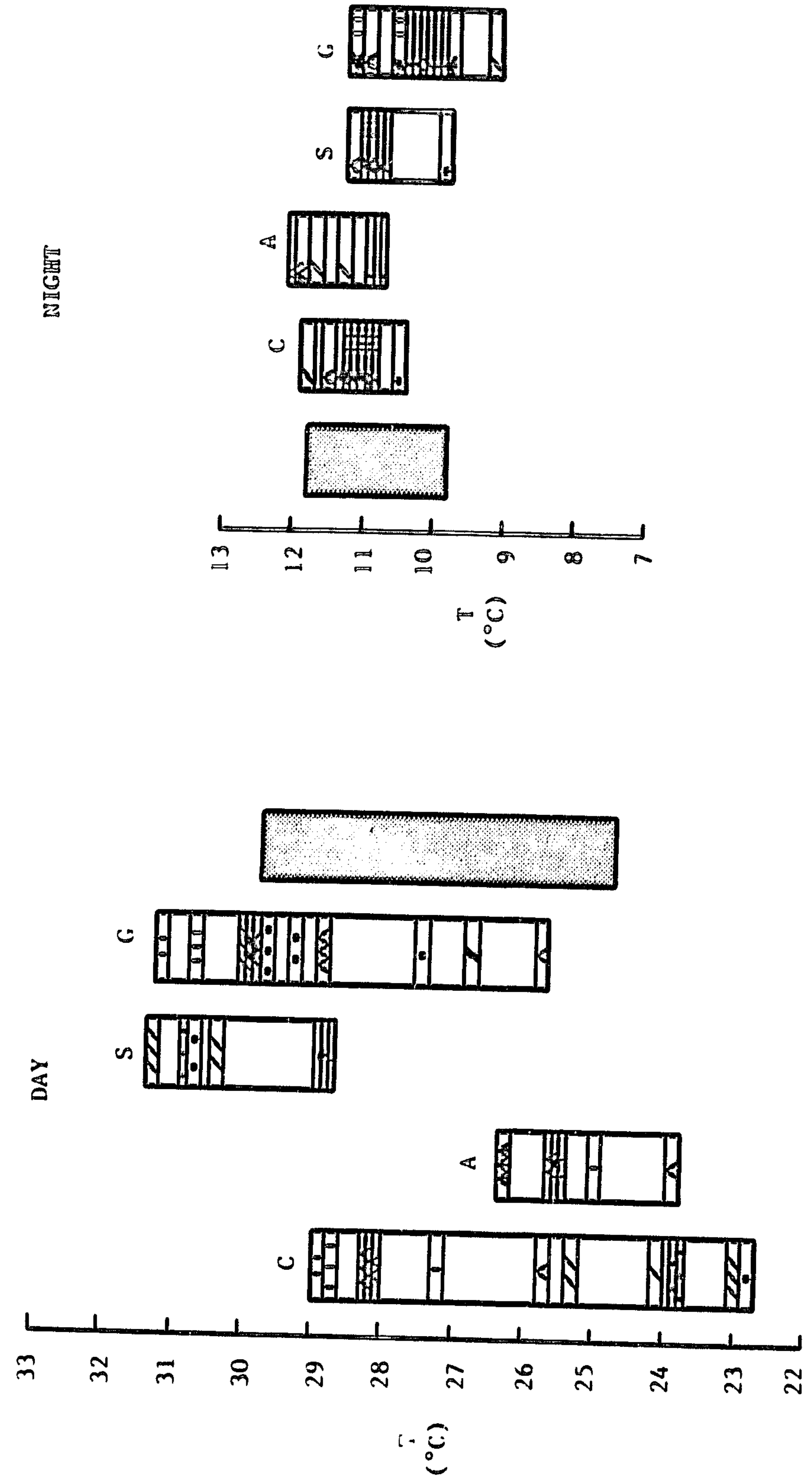
DAY
NIGHT
T (°C)
33
32
31
30
29
28
27
26
25
24
23
22
C
A
S
G
13
12
11
10
9
8
7

Figure 4.8 Surface temperature measurements for Case 7. For an explanation of the symbols see Figure 4.1.

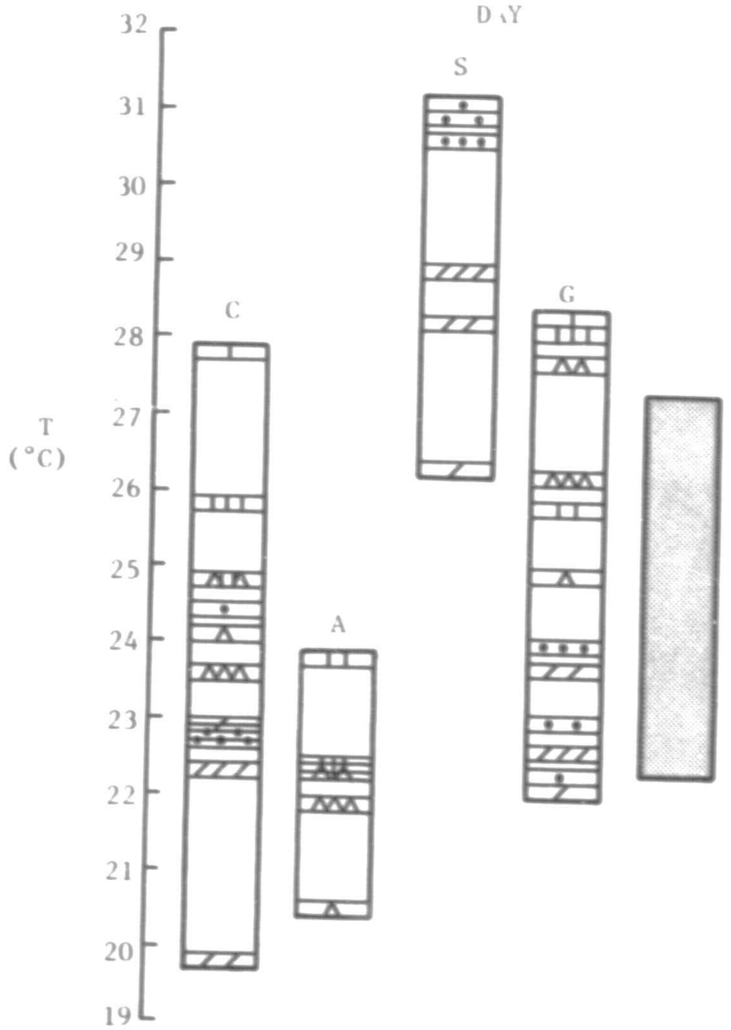
D Y
T
(°C)
32
31
30
29
28
27
26
25
24
23
22
21
20
19
C
A
S
G

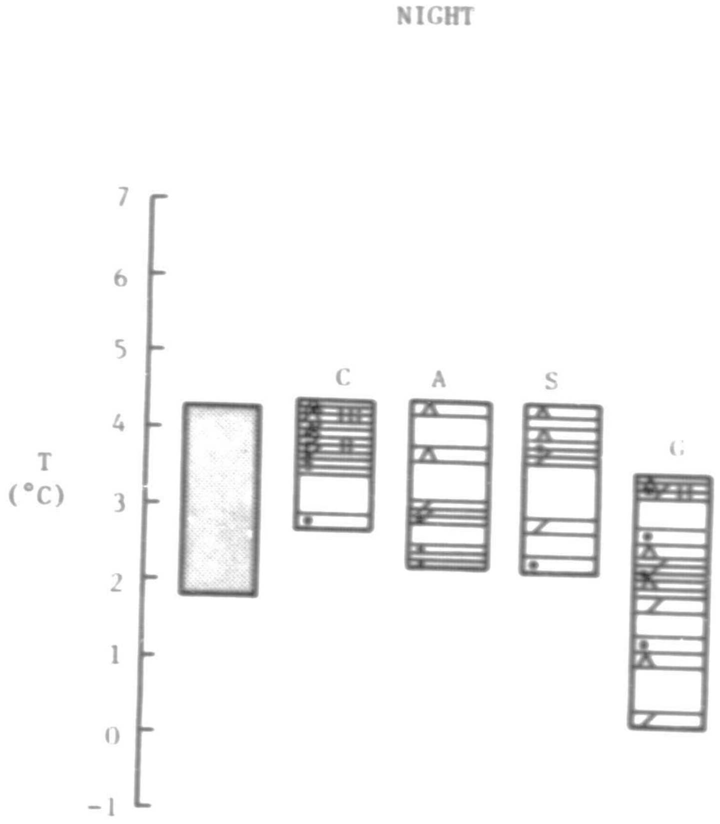
NIGHT
T
(°C)
7
6
5
4
3
2
1
0
−1
C
A
S
G

cooler readings. An examination of the 70 degree incident angle temperatures (marked with a single '.','/','∧', or ''' in Figures 4.2-4.8) shows that these temperatures were among the coolest for every crop type. The average 70 degree incident angle temperature was 1-2C cooler than the average 50 degree temperature and 1-4C cooler than the 35 degree temperature. It is clear, since the radiometer was equipped with a 20 degree field of view lens, that at an incident angle of 70 degrees the temperature reading from the radiometer viewed a portion of the horizon.

The temperature difference in row crops viewed at different solar azimuth angles found by Fuchs et al. was also present in the Rock Springs temperature data. Corn was the only row crop at the Rock Springs site, and the average corn temperature at a solar azimuth angle of 0 degrees (marked by '/','//', and '///' in Figures 4.2-4.8) is about 2C cooler than the average value measured at other azimuth angles.

The spread in the temperature data was also increased by the variety of crops at the Rock Springs site. Whether a particular crop is green and growing or brown and senecent causes a different reaction to the incident solar radiation. Radiometric measurements made by Blad and Rosenburg (1976) and Heilman and Kanemasu (1976) showed that leaf temperatures can vary between crops under the same micrometeorological conditions due to differences in evapotranspiration between the canopies. The grass at Rock Springs was characterized as "dry" in observations from all seven cases because of its brown color. Note in Figures 4.2-4.8 that the grass temperatures were consistently among the highest measured. When the soybeans were well watered and green, as in Cases 2 and 3 (Figures 4.3 and 4.4), their temperatures were some of the lowest found. In Cases 4 and 5 in September, the soybean field was characterized as "discolored (yellow) and only 25% green." This effect was caused by lack of watering during a very dry period. In the earlier cases the soybean temperatures were in the lower and middle portions of the temperature distribution. In Case 6 (Figure 4.7), the soybean temperatures were as high as the dry grass values. At this time (late September), the entire crop had dried out. Finally, in Case 7 the soybeans were harvested and only a dried stubble remained. The radiometer was then essentially viewing dry ground and the soybean temperatures were the highest values recorded in Case 7.

The large variability in the temperatures caused by the three aforementioned factors made it difficult to come up with an area-averaged value. A subjective analysis procedure was used that involved examining the temperatures as displayed in Figures 4.2-4.8 and using three guidelines:

1. The average temperature at an incident angle of 70 degrees was 1 to 4C cooler than the temperatures from the 50 and 35 degree incident angles.
2. It is the crop temperatures upwind of the sodar antenna which determine the sodar measured heat fluxes.
3. The more area a crop covered, the greater its contribution to the heat flux.

The temperature value and uncertainty for Case 1 (the shaded bar in Figure 4.2) provide an example of this process. Note that all but 2 of the 11 temperatures omitted at the low end of the error bar are from a 70 degree incident angle. The temperatures at the other extreme were eliminated for two reasons:

1. Although the soybeans covered a large area, they were located downwind of the sodar antenna.
2. Grass covered a very small portion of the site, and therefore would not have had a large effect.

This subjective analysis procedure yielded a temperature value with an uncertainty that was felt to be equivalent to two standard deviations. The shaded bars in Figures 4.3-4.8 are the estimated temperatures and uncertainties for Cases 2-7. The subjectively determined temperatures were within .5 to .15C of the average temperature of the crops upwind of the sodar antenna (alfalfa, corn, and grass) in all seven cases. Additionally, the average 50 and 35 degree incident angle temperatures of every case were within 1C of the subjective value or within the calculated uncertainty.

The nighttime temperatures are displayed in Figures 4.2-4.8 in somewhat the same manner as the daytime values, except there was no need to specify the solar azimuth angle. The average spread in the nighttime temperatures is only about 4C. The view factor problem of the 70 degree values is still present, but the vegetation has had enough time to reach a fairly uniform temperature. The nighttime temperature value and error for each case was determined through the same subjective analysis method as the daytime temperatures. However, because of the small spread of the night temperatures, the nighttime uncertainty was smaller than the daytime version. Note that no nighttime temperature data was obtained for Case 5. Thus, the value determined for Case 4 (the previous night) was used in the RDMS.

At this point, the process of calculating heat fluxes with the RDMS began. First, the boundary layer model was initialized for each case with data obtained from standard meteorological sources such as facsimile maps. Table 4.1 lists values of some of the important input variables.

The model was also initialized with a sounding that is a smoothed version of the morning (12Z) observation. During July and August 1980, radiosondes were being launched every six hours here at Penn State as part of the Northeast Regional Oxident Study (NEROS). These local sounding data were used in the first three cases. For Cases 4 through 7, the soundings from Pittsburgh (about 200 km away) were used. Since the data collection days were chosen for their lack of advection, the Pittsburgh data were considered representative of the local conditions.

Next the model was put through a 'production run' where a wide range of surface temperatures and fluxes for the same initial conditions were created by varying the values of moisture availability (M) and thermal inertia (P). The output from a 'production run' of the model was used to create a set of regression equations. These regression equations inverted the model output and thus were able to predict values of M and P for every case from the observed day and night temperatures. The predicted M's and P's were then used to calculate the RDMS heat fluxes. The model was run again for each case using the same set of initial conditions, but M and P were fixed at their predicted values. The heat flux curve from this model run was taken as the RDMS heat flux estimate for a given case. Appendix C contains an example of the process for determining a heat flux estimate.

Table 4.1 Model input parameters for each case.

Case	Ground Temperature (°K)	Temperature at 50m (°K)	Roughness Length (m)	Mean Wind 0 to 5m (m/sec)	Mixing Ratio at 50m	Precipitable Water (m)	Albedo	Emissivity
1	288.2	289.5	.20	3.00	.012	.015	.15	1.0
2	287.2	288.2	.20	3.00	.011	.018	.15	1.0
3	288.3	289.6	.20	3.0	.012	.016	.15	1.0
4	283.3	284.0	.20	2.7	.008	.013	.15	1.0
5	280.5	281.8	.20	4.0	.007	.013	.15	1.0
6	281.4	282.2	.20	3.5	.007	.015	.15	1.0
7	283.2	284.4	.20	3.0	.008	.015	.15	1.0

In order to project the uncertainty in the temperature values through the RDMS, day and night temperatures from either end of their respective error bars were used to create two additional day/night temperature pairs for every case. The results from calculations with the extreme temperature pairs thus defined the uncertainty in the RDMS M, P, and heat flux values.

4.3 SODAR DATA ANALYSIS

In Section 2.2 it was shown that under free convection conditions, C_T^2 is related to the heat flux in this fashion:

$$C_T^2 = \frac{3}{4} \left(\frac{\overline{T}}{kg}\right)^{2/3} \left(\frac{H_o}{\rho C_p}\right)^{4/3} Z^{-4/3} \tag{4.1}$$

The result of taking the logarithm of this equation is a linear relationship between log C_T^2 and log Z.

$$\log C_T^2 = \log \left[\frac{3}{4} \left(\frac{\overline{T}}{kg}\right)^{2/3} \left(\frac{H_o}{\rho C_p}\right)^{4/3}\right] - 4/3 \log Z \tag{4.2}$$

Note that the slope of this line is -4/3 and the intercept A is

$$A = \log \left[\frac{3}{4} \left(\frac{\overline{T}}{kg}\right)^{2/3} \left(\frac{H_o}{\rho C_p}\right)^{4/3}\right] \tag{4.3}$$

Free convection is usually confined to a layer of the atmosphere several hundred meters deep. Thus, only a section of a log-log plotted C_T^2 profile will have the characteristic -4/3 slope present if free convection exists (see Figure 4.9). A straight line with a -4/3

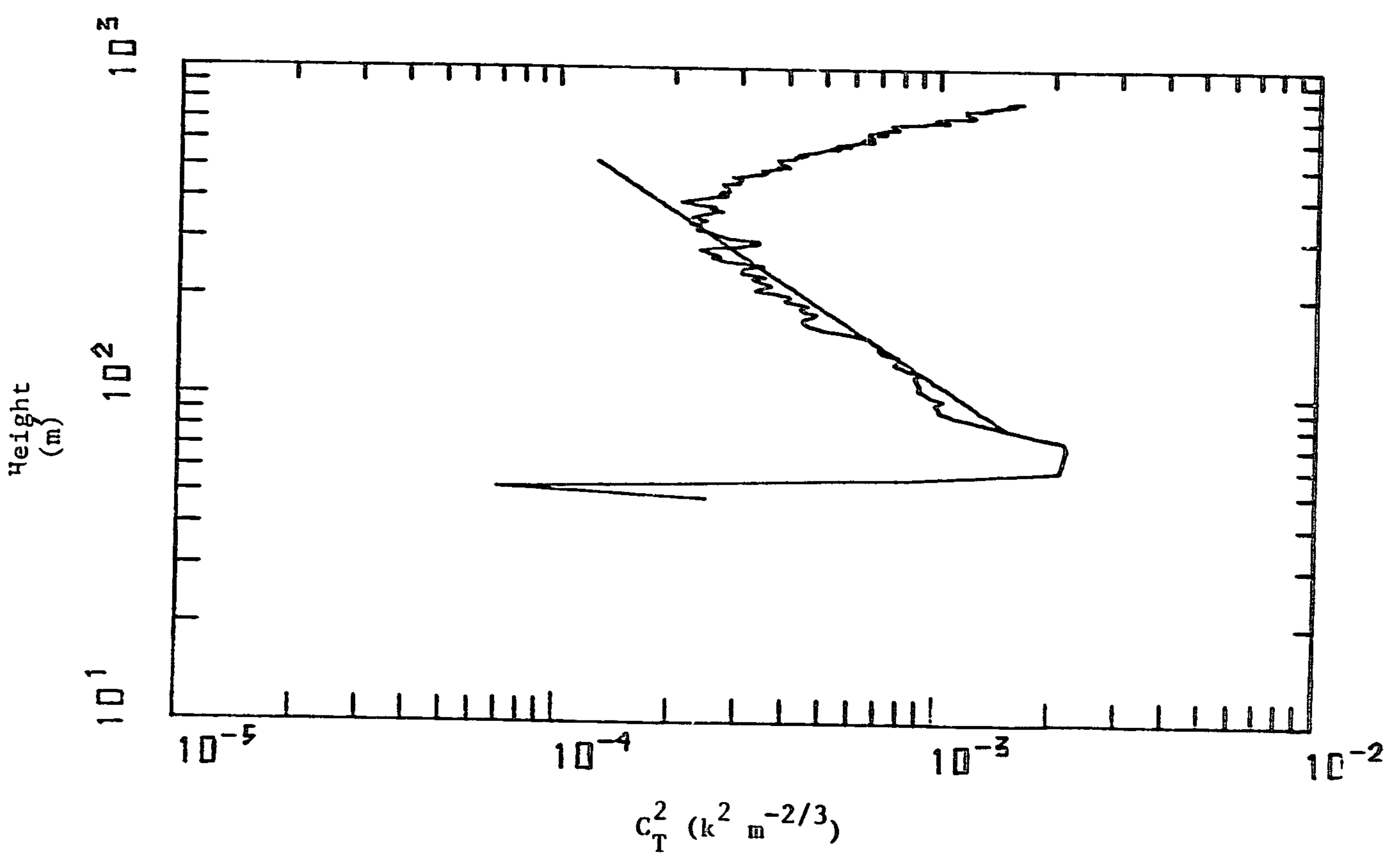

Figure 4.9 Example of a log-log plot of C_T^2 versus height exhibiting the characteristic -4/3 slope of free convection.

slope can then be fit to that portion of the profile, and the value of the intercept is used to produce a heat flux estimate.

Using the sodar data collected from every case, C_T^2 values were calculated and then averaged over each ten minute period from 900 to 1700 EST. From those averages, the log-log plots of C_T^2 versus height were produced. When a portion of a profile showed a -4/3 slope, a 'nomogram' of lines with a -4/3 slope and various intercepts calibrated in values of heat flux was placed over the C_T^2 profile. Figure 4.10 is an example of a 'nomogram' that goes from values of 5 to 60 W m^{-2} by increments of 5 W m^{-2}. The average heat flux for that ten-minute period based on the free convection section of the profile was calculated using the 'nomogram'.

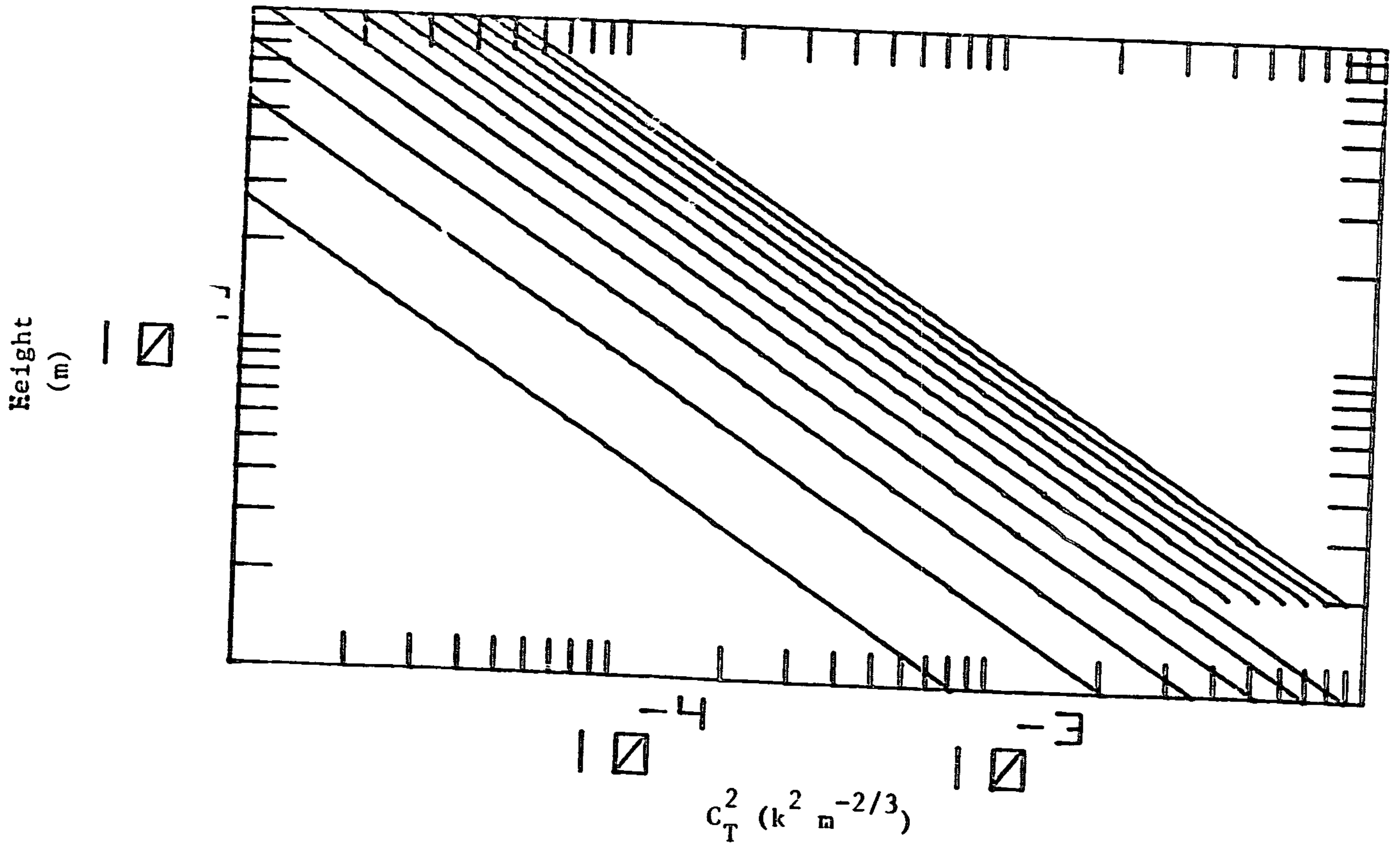

Figure 4.10 'Nomogram' of lines with a -4/3 slope and various intercepts calibrated to read from 5 to 60 W m^{-2} in increments of 5 W m^{-2} starting at the left side.

5.0 RESULTS

5.1 INTRODUCTION

The results from this research need to be discussed in terms of two separate measurement periods:

1. The first three data sets collected in mid- and late July. (Hereafter referred to as the J cases.)
2. The last four data sets taken during mid-September and early October. (Hereafter referred to as the S cases.)

An examination of the heat flux estimates from both the sodar and the SDMS suggests significant differences between the two periods. In the S cases, no usable sodar values of heat flux were obtained due to the absence of a clear-cut free convection regime, whereas the SDMS estimates of heat flux increased between the J and S cases. In the discussion below, three primary causes for variations in surface heat flux between the J and S cases are evaluated:

1. The change of season.
2. The aging of the crop between the two periods.
3. The change in the soil moisture between July and September.

5.2 RADIOMETRIC/MODEL DERIVED HEAT FLUXES

Figure 5.1 displays the surface temperature ranges for every case. Between the J and S cases there is a drop of 6C and 7C in the average day and night temperatures, respectively. This step change is caused by the seasonal decrease in the amount and intensity

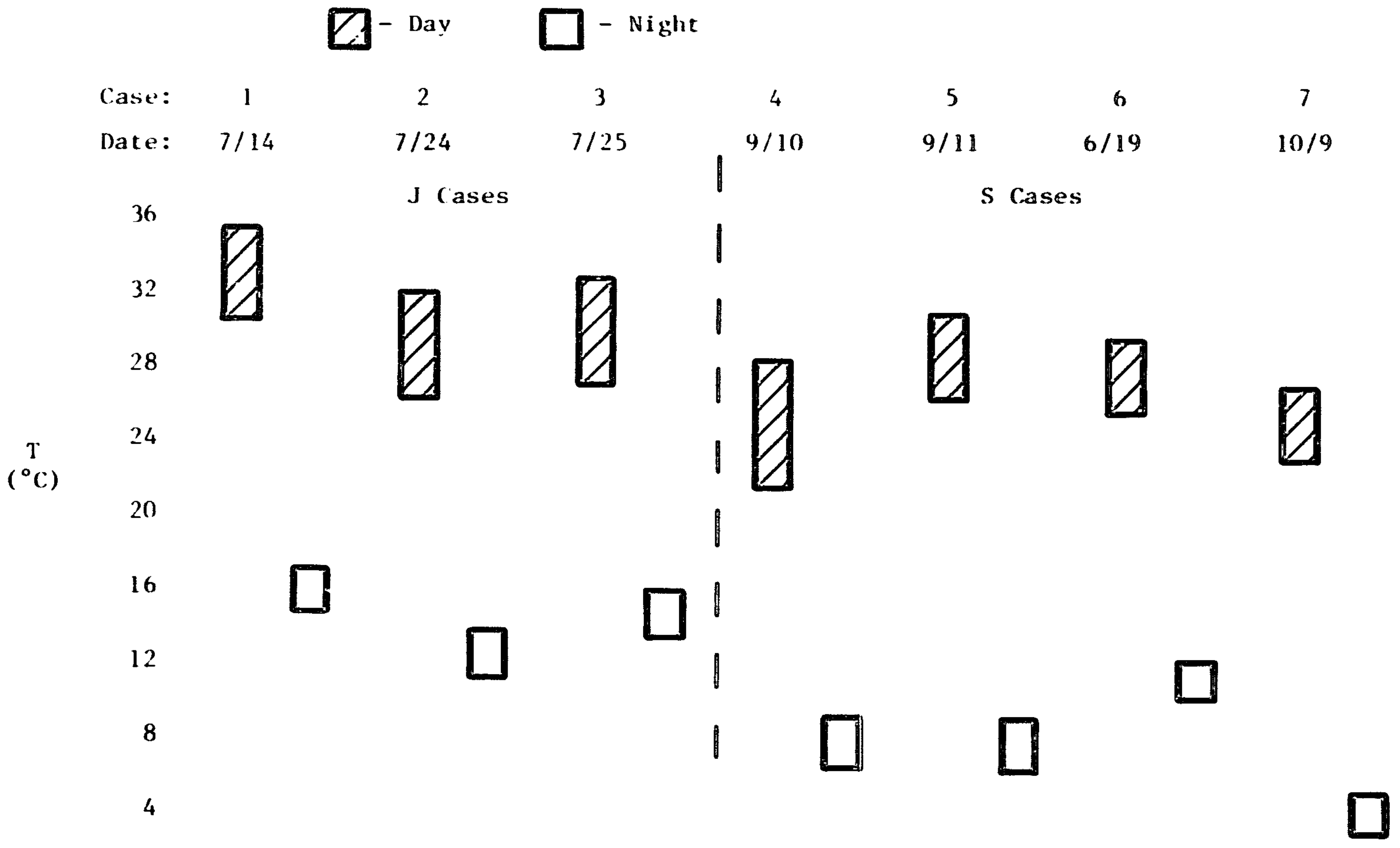

Figure 5.1 Day and night surface temperature ranges calculated for Cases 1-7.

of solar radiation. Solar radiation records from the Penn State Meteorological Observatory showed 482 W m^{-2} received on July 25 (Case 3) versus 422 W m^{-2} on September 11 (Case 4). The zenith angle of the sun was larger in the S cases, resulting in a decrease in the intensity of the solar radiation. Although the temperature ranges for the S cases were cooler, the RDMS heat fluxes (see Figure 5.2) increased an average of 25 W m^{-2} between the J and S cases. Apparently, although the solar radiation was weaker in the S cases, it was partitioned in such a manner as to produce heat fluxes greater than those in the J cases. There is evidence that a reduction in the evaporative flux is responsible for this result.

Along with the amount of rainfall, the age of the plants is an important factor determining the evaporation from a canopy. When vegetation becomes senecent, reaching the end of its life cycle, evapotranspiration is greatly reduced. Observations indicated that senecent vegetation and a lack of rainfall were present in the S cases.

Since the S cases occurred in the autumn, the crops at Rock Springs were brown and dying. To quantify the lack of rain in the S cases, an Antecedent Precipitation Index (API) was calculated for each case from the rainfall data at the Penn State Meteorological Observatory. The API, following Blanchard et al., (1980)[1], expresses moisture depletion as an exponential decaying function of the rainfall in this form,

---

[1] Blanchard, B. J., McFarland, M. J., Schmugge, T. J., and Rhoades, E.: "Estimation of soil moisture with API algorithms and microwave emissions." Unpublished manuscript.

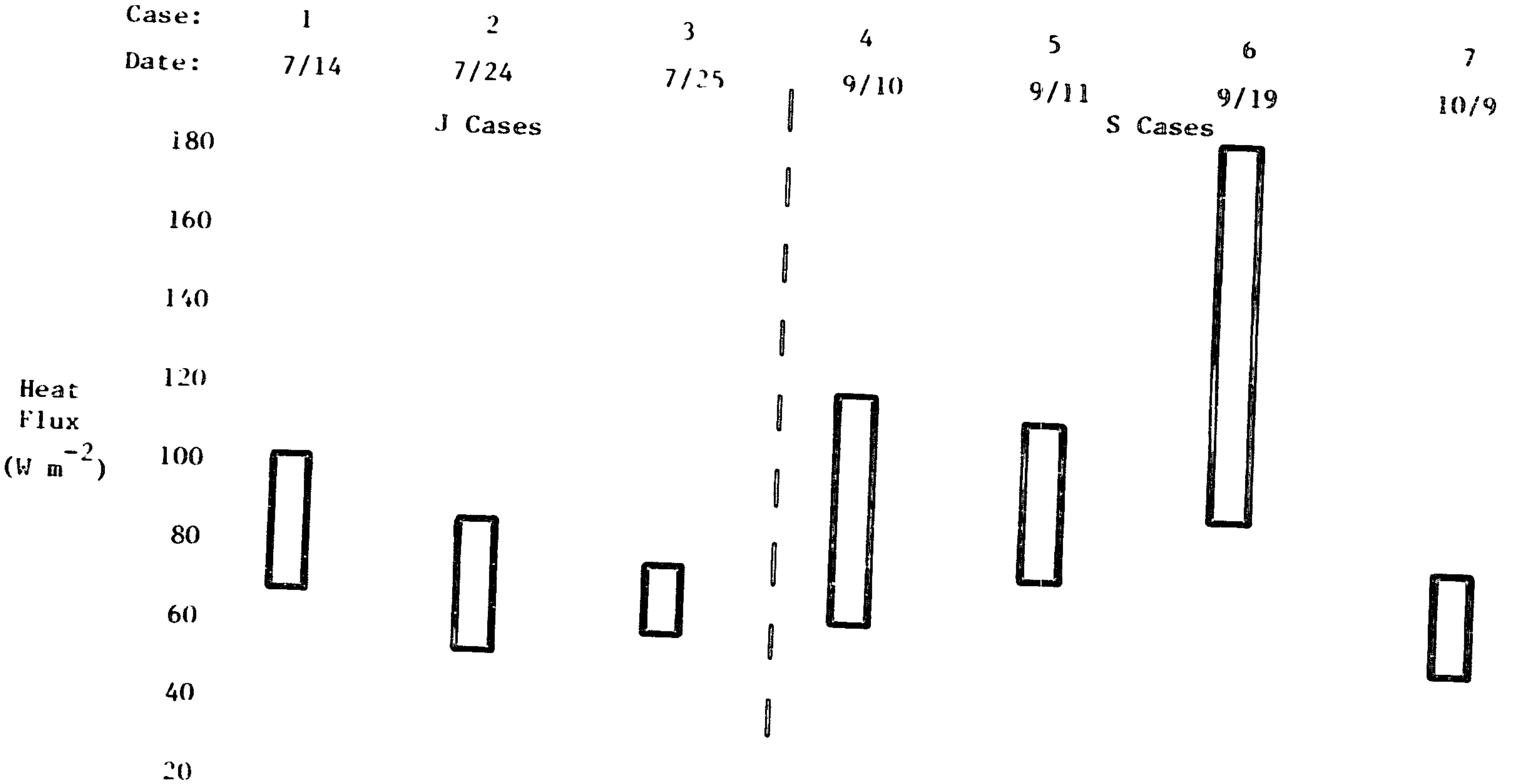

Figure 5.2 The average heat flux for 1400-1430 EST for Cases 1-7.

$$API_i = P_i + (API_{(i-1)})\, k_i \tag{5.1}$$

where

API = moisture index

P = daily effective rainfall

k = depletion constant < 1 and a function of time

i = day of the estimate.

An average depletion constant (k) for the period of .920 was used and the effective rainfall P was related to the actual rainfall P_a in this fashion:

$$P = P_a^{.829} \tag{5.2}$$

The API values for each case are displayed in Figure 5.3. The average API in the S cases is one-half the value in the J cases.

This change in soil and crop moisture was reflected in the RDMS measurements. Figure 5.4 is a block diagram of the RDMS M and P values for every case. Note that the average RDMS estimate of M for the S cases decreases by three tenths from the J cases. When the moisture availability of a surface decreases, a larger amount of the net radiation is partitioned into sensible heat flux instead of evaporative flux. By examining the RDMS-computed Bowen ratios for each case (Figure 5.5), the change in the partitioning of the net radiation between the J and S cases is clearly demonstrated.

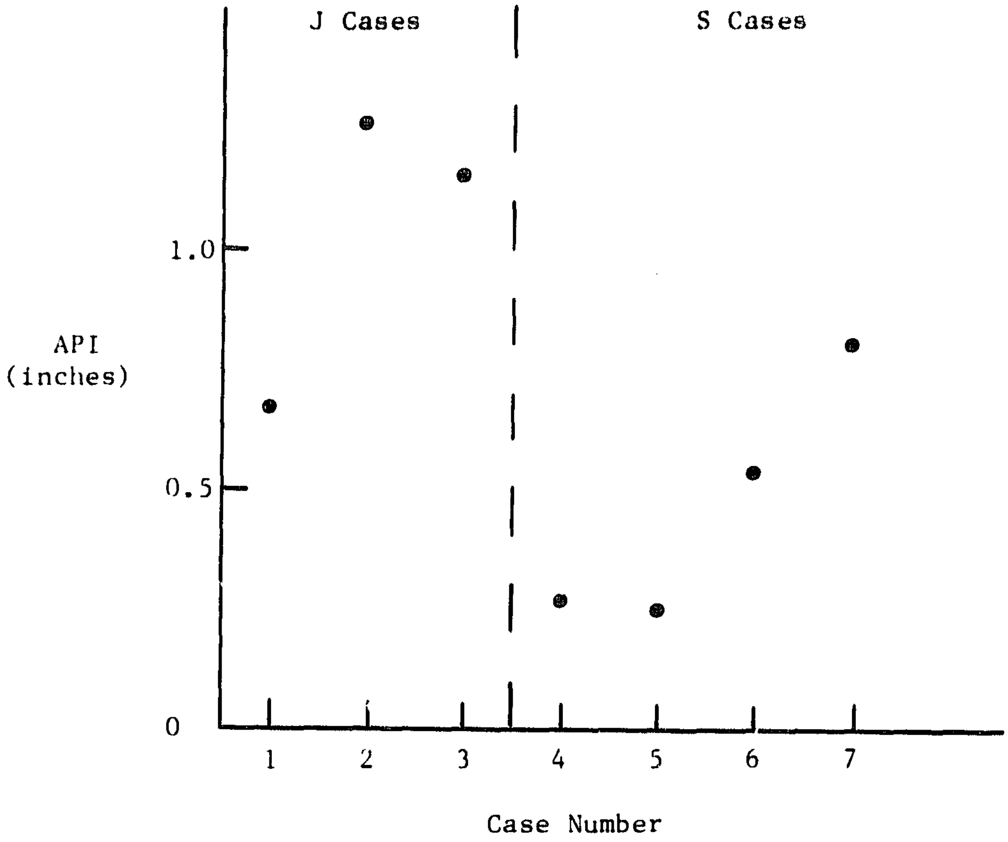

Figure 5.3 The Antecedent Precipitation Index (API) for each case. An average depletion constant (k) of .92 was used.

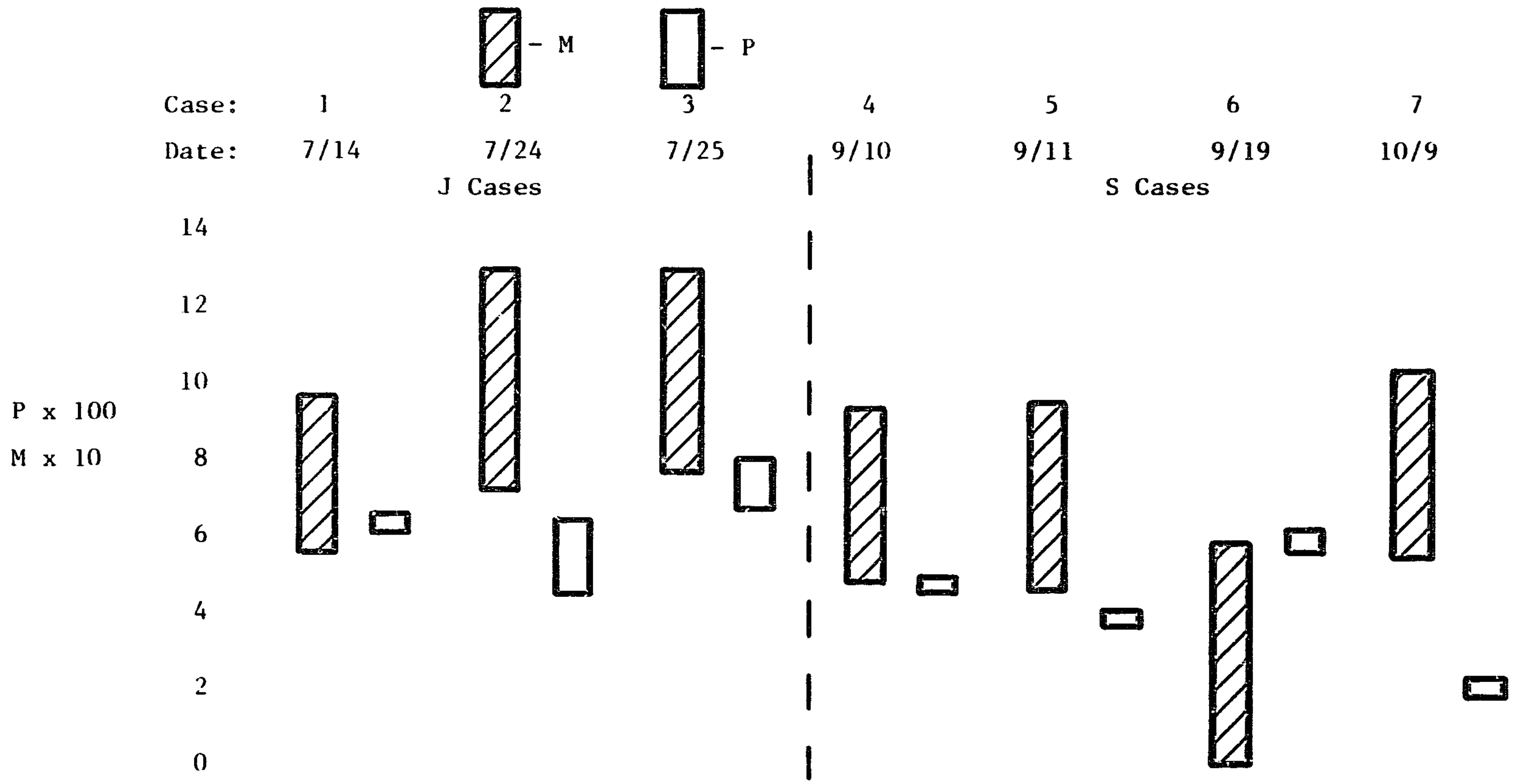

Figure 5.4 Estimates of the moisture availability (M) and thermal inertia (P) calculated by the RDMS for Cases 1-7.

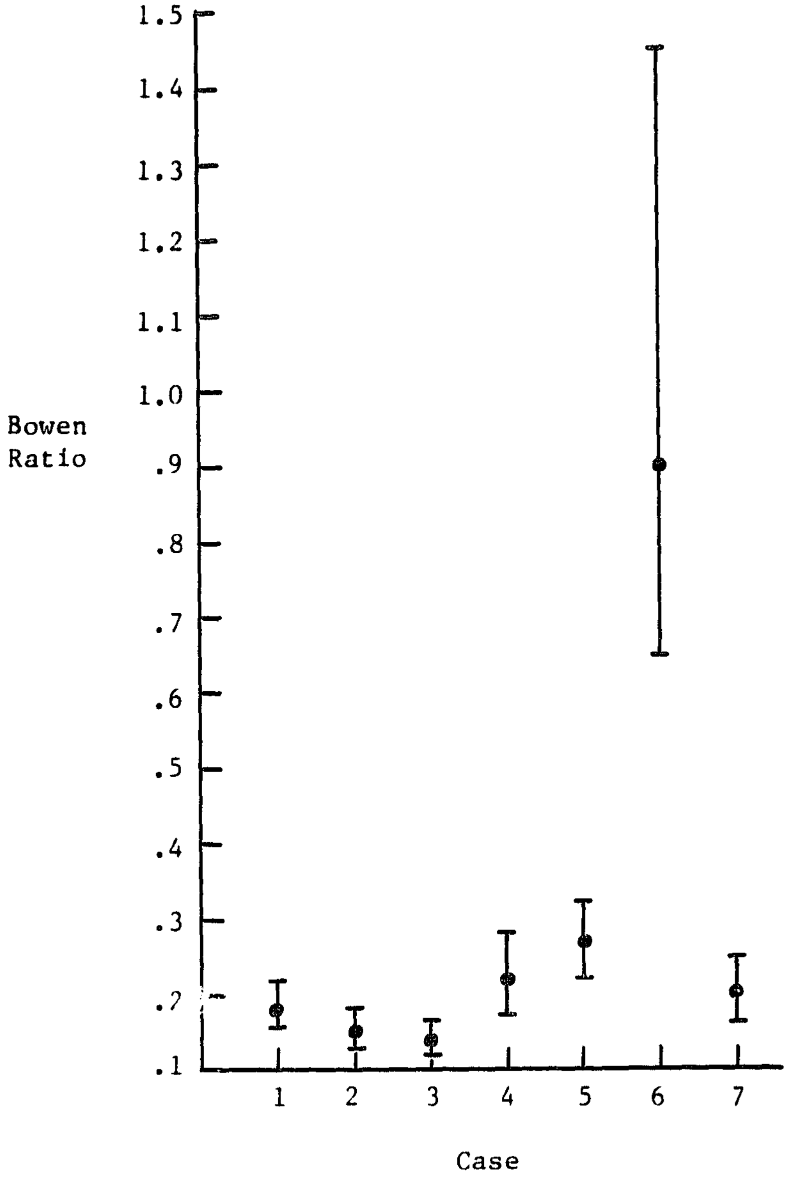

Figure 5.5 Bowen ratios calculated by the RDMS for Cases 1-7.

5.3 SODAR DERIVED HEAT FLUXES

When the sodar data were first analyzed, the C_T^2 profiles produced were 30 minute averages. Very few -4/3 slopes that extended over 100 meters were observed in any of the cases. Figure 5.6 illustrates the state of the atmosphere when free convection exists. A matching layer where both surface and mixed layer scaling are valid is present from a height of the absolute value of the Monin Length (L) to one tenth of the inversion height (.1 Z_i). A matching layer is most often found when winds are light, and solar heating is strong. Thus, the absence of extensive -4/3 slopes in the C_T^2 profiles was puzzling because of the clear skies and light winds (3-5 m/s) present when the data were collected.

The original intent of the 30-minute averages was to eliminate the effects of individual thermals and thereby show the average free convection layer. It appeared from the 30-minute averages however, that only a small portion, if any, of most 30-minute periods had free convection conditions existing. To see if free convection periods were present on a shorter time scale, C_T^2 profiles averaged over 10-minutes were produced for all the cases. The 10-minute averages indicated that the sodar heat fluxes were also divided into J and S cases. With the sodar, however, the difference was much more drastic since the 10-minute averages improved the heat flux estimates in the J cases but failed to produce better results in the S cases.

Although the J cases showed deeper free convection with the 10-minute averages, free convection was still present only intermittently throughout the day. The inconsistent presence of free convection in

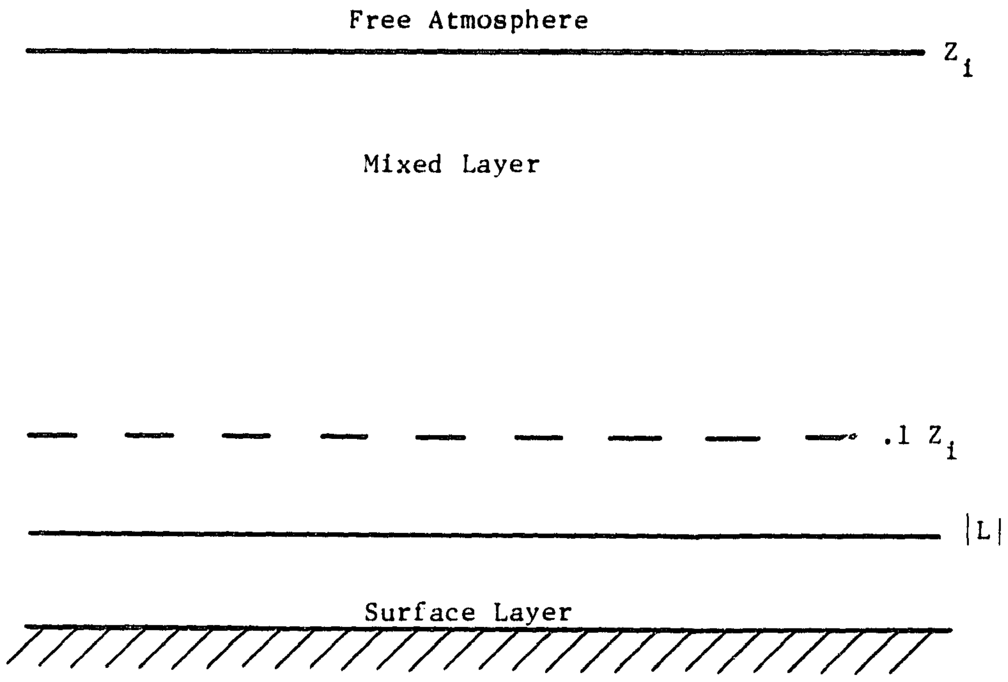

Figure 5.6 A schematic diagram of the atmosphere when free convection conditions exist.

the J cases is illustrated by examination of two of the log-log plots of C_T^2 versus height used to estimate the heat flux. Figure 5.7a is the average C_T^2 profile for 1350-1400 EST on July 24 (Case 2), and Figure 5.7b is the average profile for the following ten minutes. It should be noted that the -4/3 slope line drawn on each plot is not the best linear fit to the -4/3 slope over the entire depth of the free convection layer, but merely a line drawn through the C_T^2 value at 150 m to illustrate the -4/3 slope. Figure 5.7b has a free convection layer extending from 80 to 200 meters, while that for the previous ten-minute average indicates a shallow layer of about 30 m at a height of 150 m. This lack of continuous free convection is present throughout the J cases.

In the S cases, the situation was even worse. Occasional free convection periods were noted in the early morning hours (900-1100 EST), but were lacking in the remainder of the day. Figure 5.8 is a C_T^2 profile for 1400-1410 EST on September 11 (Case 4) showing the weak C_T^2 values characteristic of an S case afternoon. Thus, any heat fluxes that were determined in the S cases were weak and failed to display a diurnal trend. The lack of the expected diurnal variation increased doubts about obtaining any useful heat fluxes from the S cases' sodar data.

Obviously something was disrupting the establishment of continuous free convection conditions at the site of sodar antenna. A mixed layer depth experiment using aircraft and sodar measurements had been performed at Rock Springs in 1978 (Lipschutz, 1978). Underwood (1981b) noted the presence of a low level inversion in the sodar data below the inversion height measured from the aircraft. In order to see if

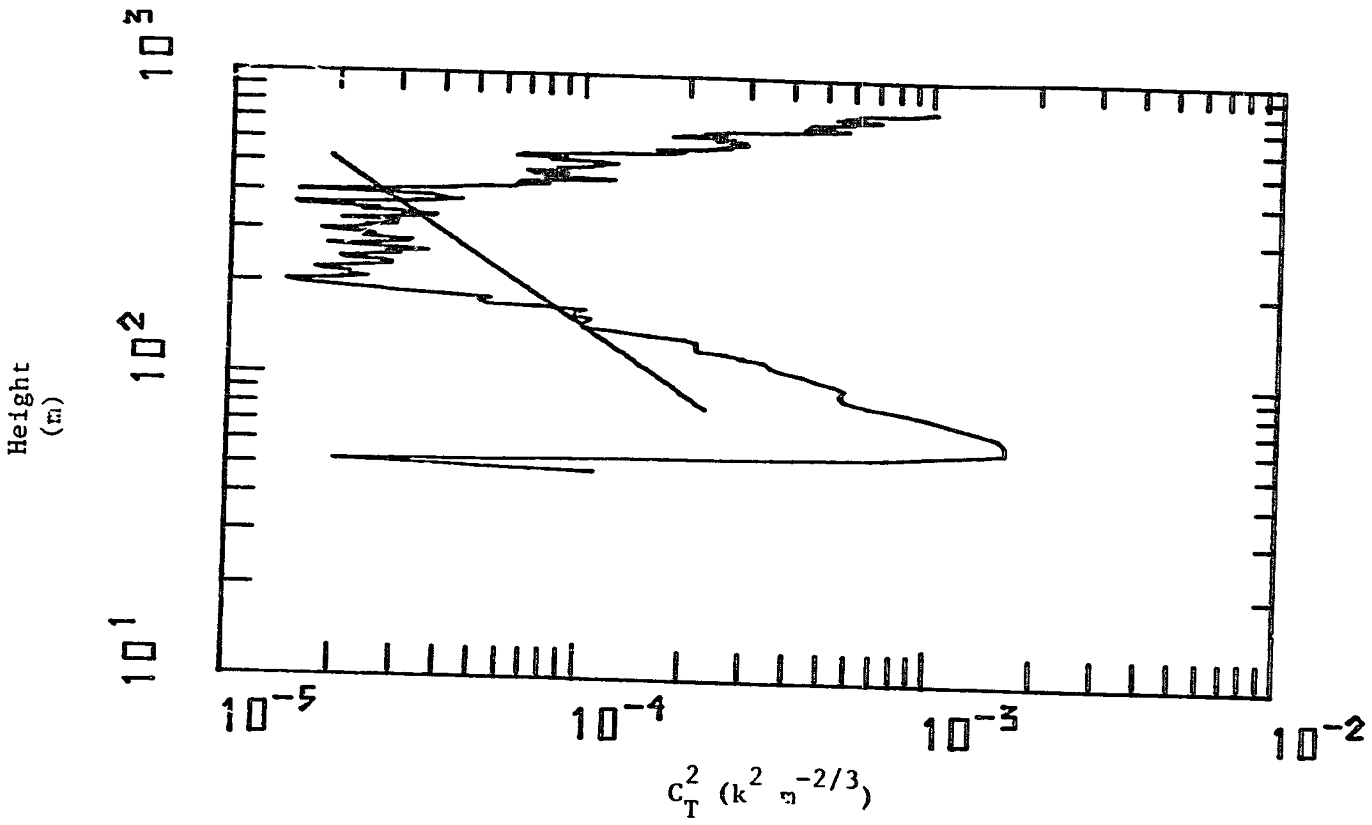

Figure 5.7a The average C_T^2 profile for 1350-1400 EST in Case 2.

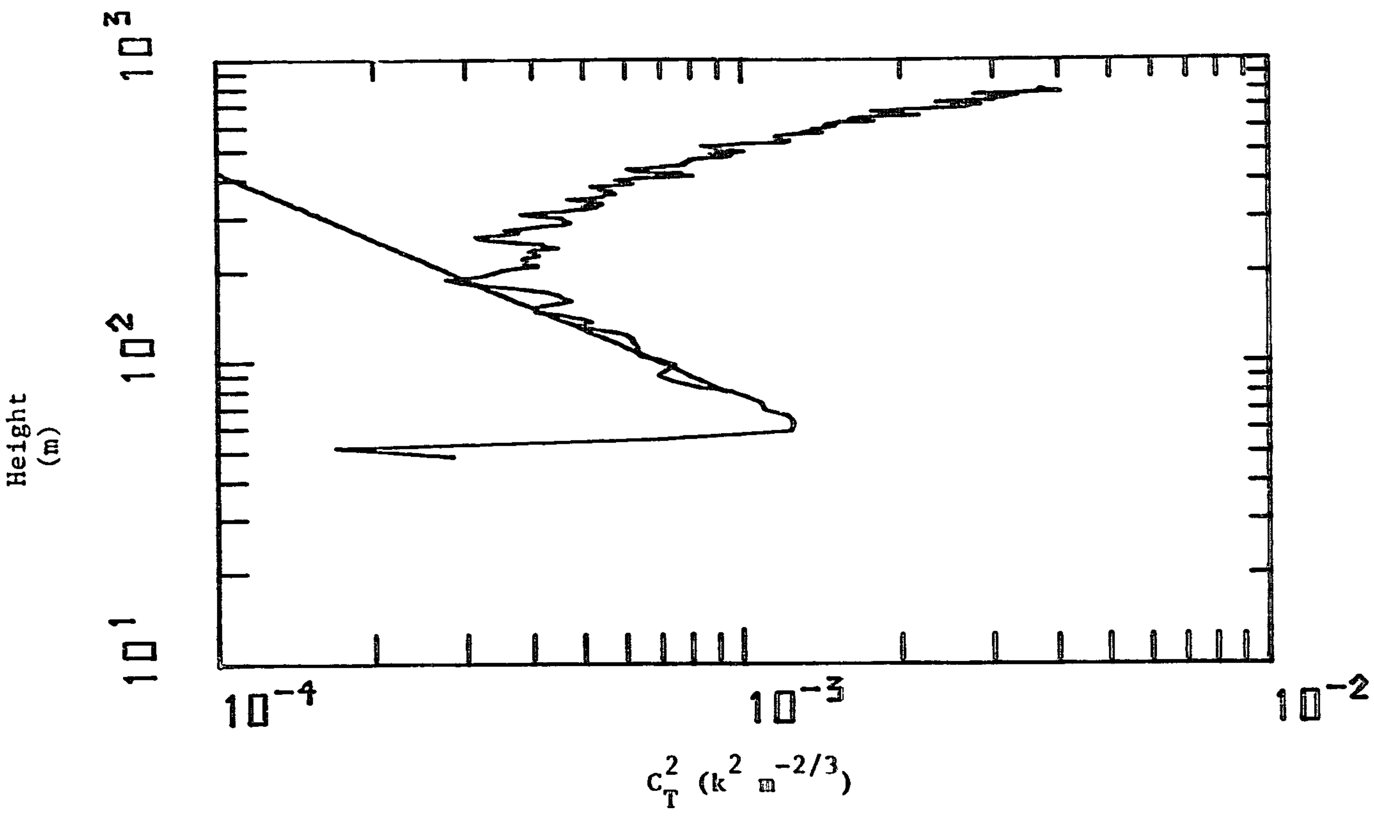

Figure 5.7b The average C_T^2 profile for 1400-1410 EST in Case 2.

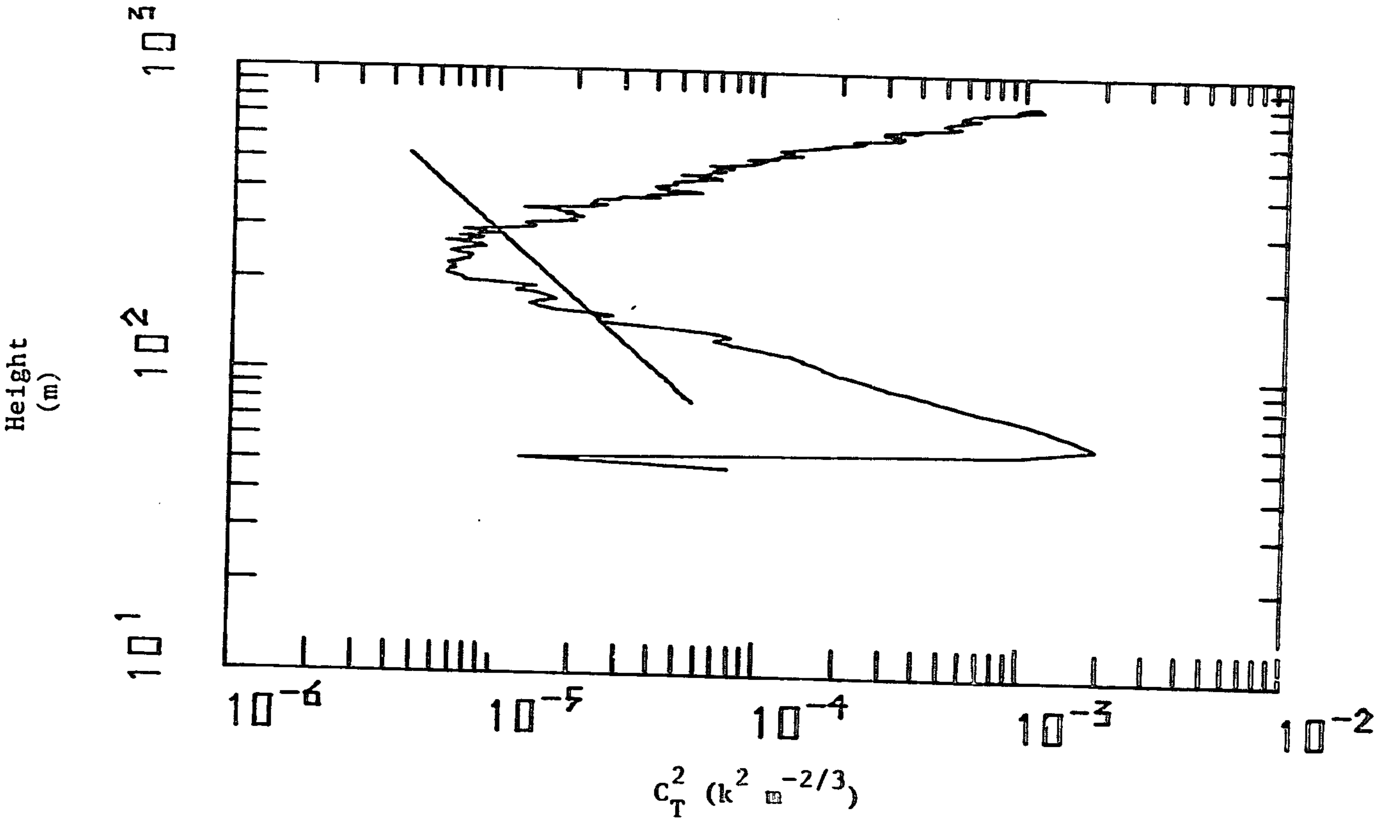

Figure 5.8 The average C_T^2 profile for 1400-1410 EST from Case 4 (September 20).

a low level inversion was present in this experiment, the six hourly NEROS sounding data taken at Penn State during Cases 2 and 3 (July 24 and 25) were examined. Figure 5.9 includes the series of soundings for Case 3 (July 25). Note the weak inversion at 920 mb in the afternoon (18Z) sounding that is still present in the evening (00Z) sounding. Thus, even during the strong solar radiation of the J cases a low level inversion was present.

Speculation on the cause of this inversion centered on the non-homogeneity of the terrain surrounding the site. As Figure 5.10 shows, the sodar is located on the east side of a broad valley. To the west are a ridge and elevated plateau. When the western ridge and plateau were heated, a plume of warm air at the surface of the plateau could have been advected by northerly winds at levels above the valley floor[2]. This elevated plume was a possible cause of the low level inversion plaguing the sodar results.

The intermittent nature of the free convection conditions in the J case sodar data indicated that the low level inversion might periodically be disrupted by the penetration of a large thermal. At that time, short-lived free convection would exist and the sodar could estimate the heat flux. Figure 5.11 shows the quantitative false color display of the sodar data from Case 2 (July 24) and Case 6 (September 19). As shown by the Case 2 sodar returns, strong thermals were rising from the surface to about 200 m, whereas in Case 6 there was only weak thermal activity. The conclusion is that because of the reduced solar radiation in the S cases, the thermals

---

[2] Observed winds were northerly during every case.

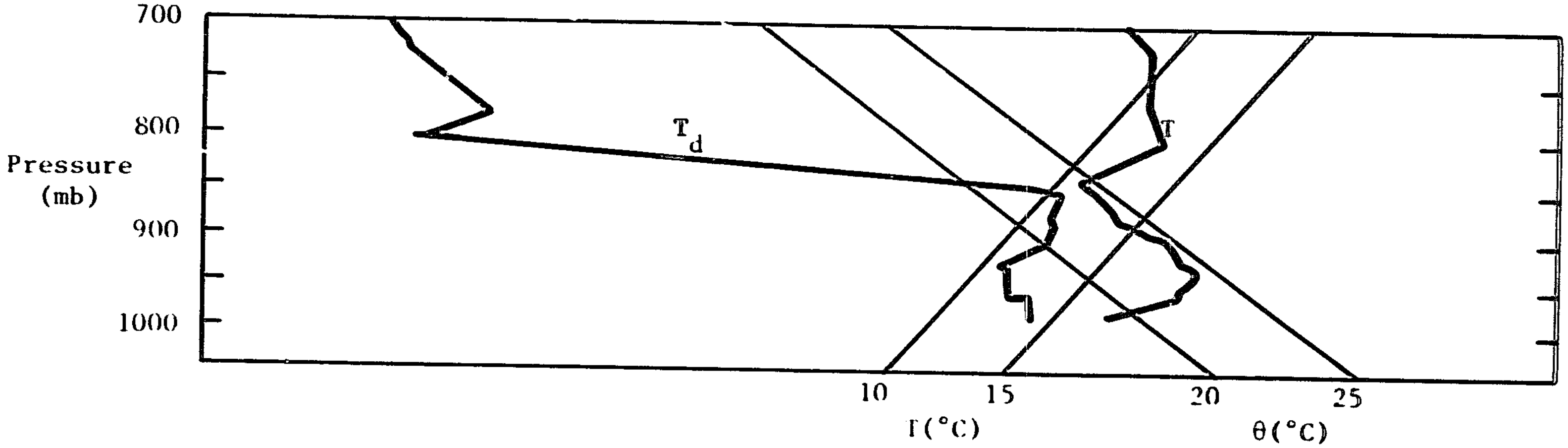

Figure 5.9a The NEROS sounding taken at Penn State for 700 EST 25 July 1980 (Case 3).

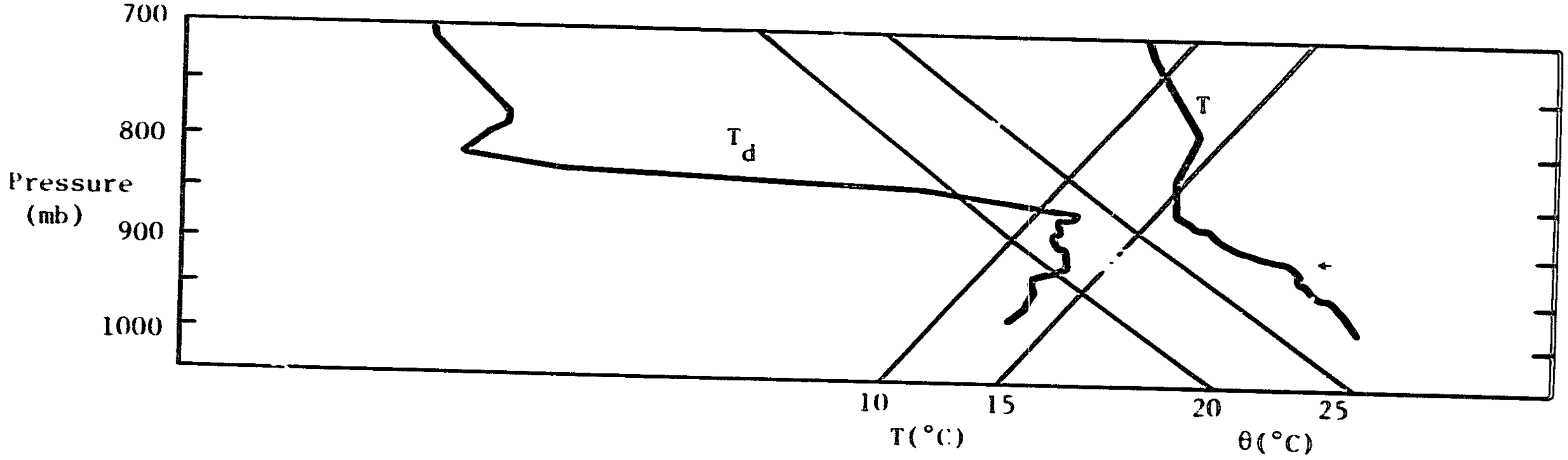

Figure 5.9b The NEROS sounding taken at Penn State for 1300 EST 25 July 1980 (Case 3).

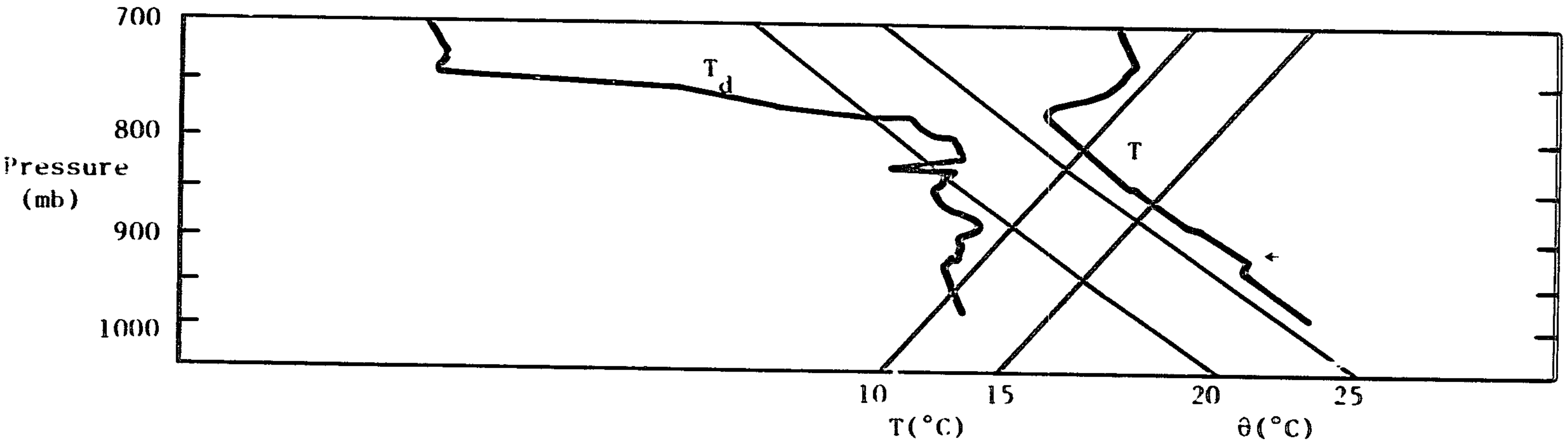

Figure 5.9c The NEROS sounding taken at Penn State for 1900 EST 25 July 1980 (Case 3).

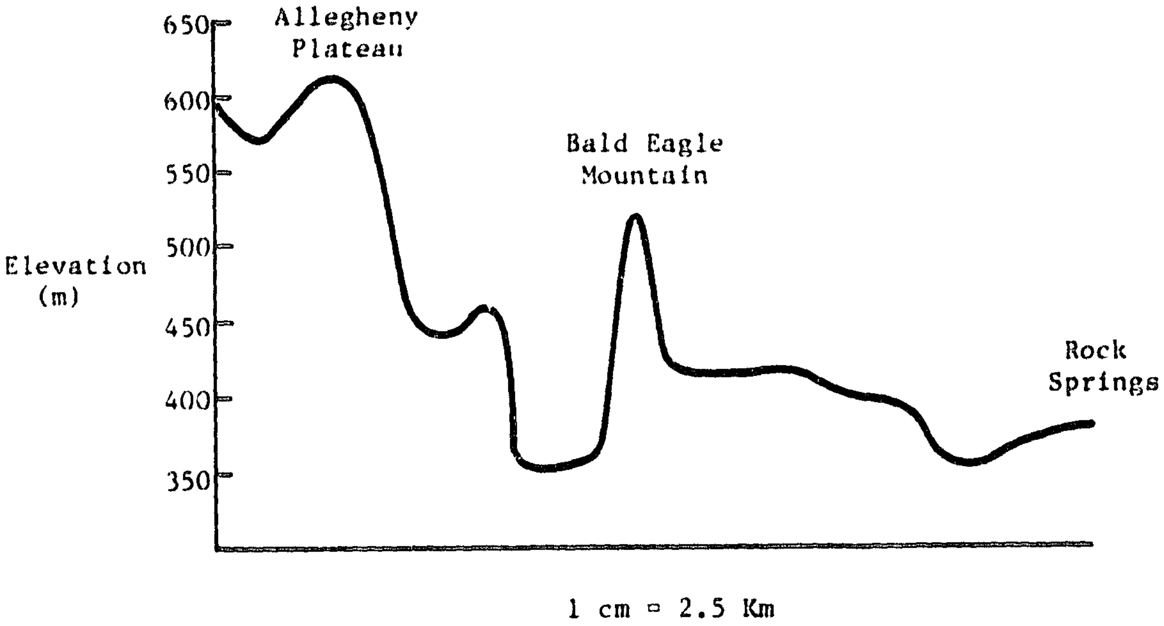

Figure 5.10 Terrain profile northwest of Rock Springs.

ORIGINAL PAGE
BLACK AND WHITE PHOTOGRAPH

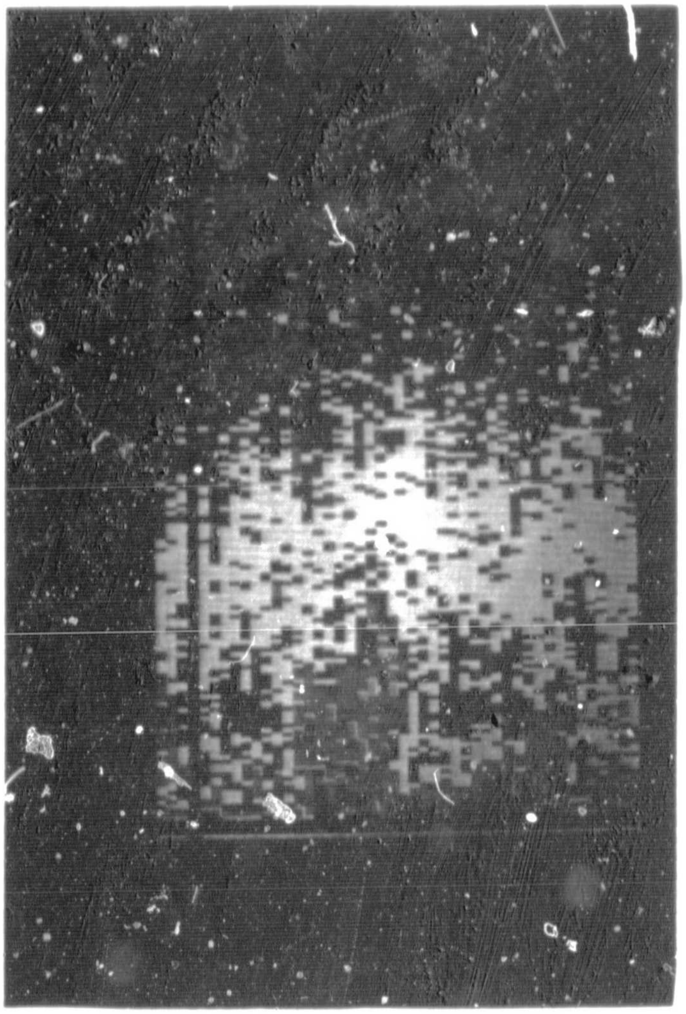

White and Red = highest C_T^2 values.

Black and Blue = lowest C_T^2 values.

Date, time and location are displayed vertically near the left side.

The scale on the left side is in hundredths of meters.

Figure 5.11a Quantitative false color display of sodar data for Case 2.

ORIGINAL PAGE
BLACK AND WHITE PHOTOGRAPH

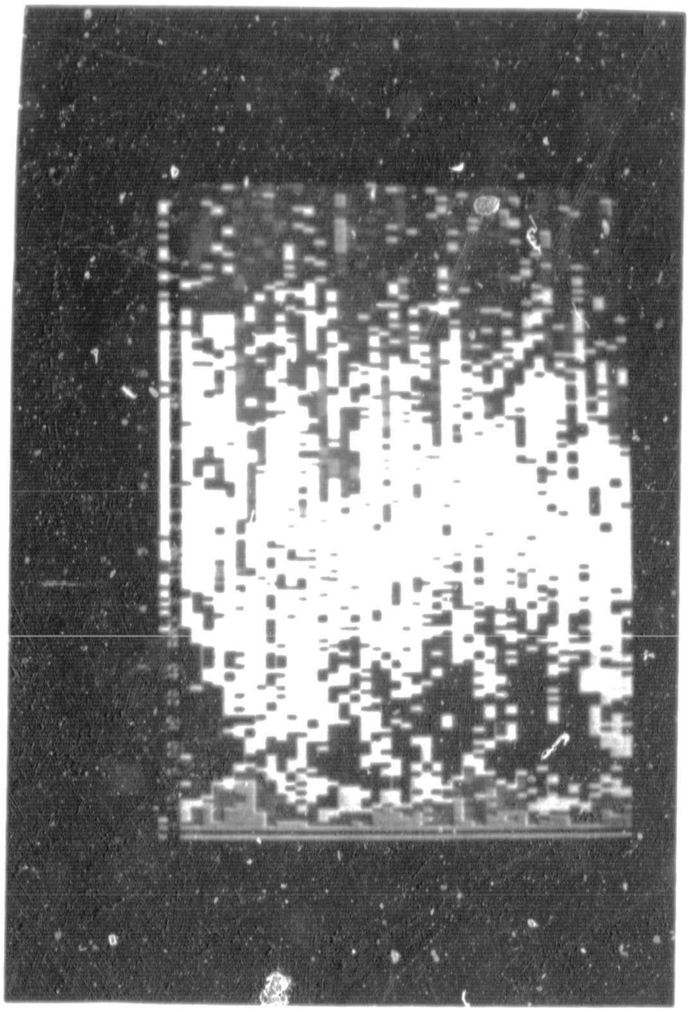

White and Red = highest C_T^2 values.

Black and Blue = lowest C_T^2 values.

Date, time and location are displayed vertically near the left side.

The scale on the left side is in hundredths of meters.

Figure 5.11b Quantitative false color display of sodar data for Case 6.

were weaker than in the J cases and were never able to break the inversion. Since a free convection layer could not be established, no heat flux estimates could be made from the S cases' sodar data.

5.4 COMPARISON OF THE SDMS AND SODAR HEAT FLUXES

Because the sodar heat flux values from Cases 4-7 were considered unreliable, the comparison between the RDMS and sodar values was attempted only for Cases 1-3. Figures 5.12-5.14 display the RDMS heat flux and solar radiation estimates compared with sodar heat flux and pyranometer data, respectively.

The uncertainty in the RDMS heat flux estimates was caused by the problems in determining an area-averaged temperature for the heterogeneous Rock Springs site. There were three day/night temperature pairs for each case that defined the estimated area-averaged value and its error. The three heat flux curves produced from those temperatures therefore defined the RDMS heat flux estimate and its uncertainty. In Figures 5.12-5.14, the RDMS heat flux is plotted as a swath with boundaries that lie halfway between the RDMS heat flux curve and the curves defining its uncertainty. The high and low heat flux curves themselves were not plotted as the error limits because those curves were often based on extreme values of M. For example, the low heat flux curve of Case 1 is calculated using an M value slightly greater than 1. Thus, the most reasonable uncertainty for the RDMS heat flux was felt to be halfway between the middle curve and each extreme curve.

The sodar heat flux values plotted in Figures 5.12-5.14 were corrected for three known error sources:

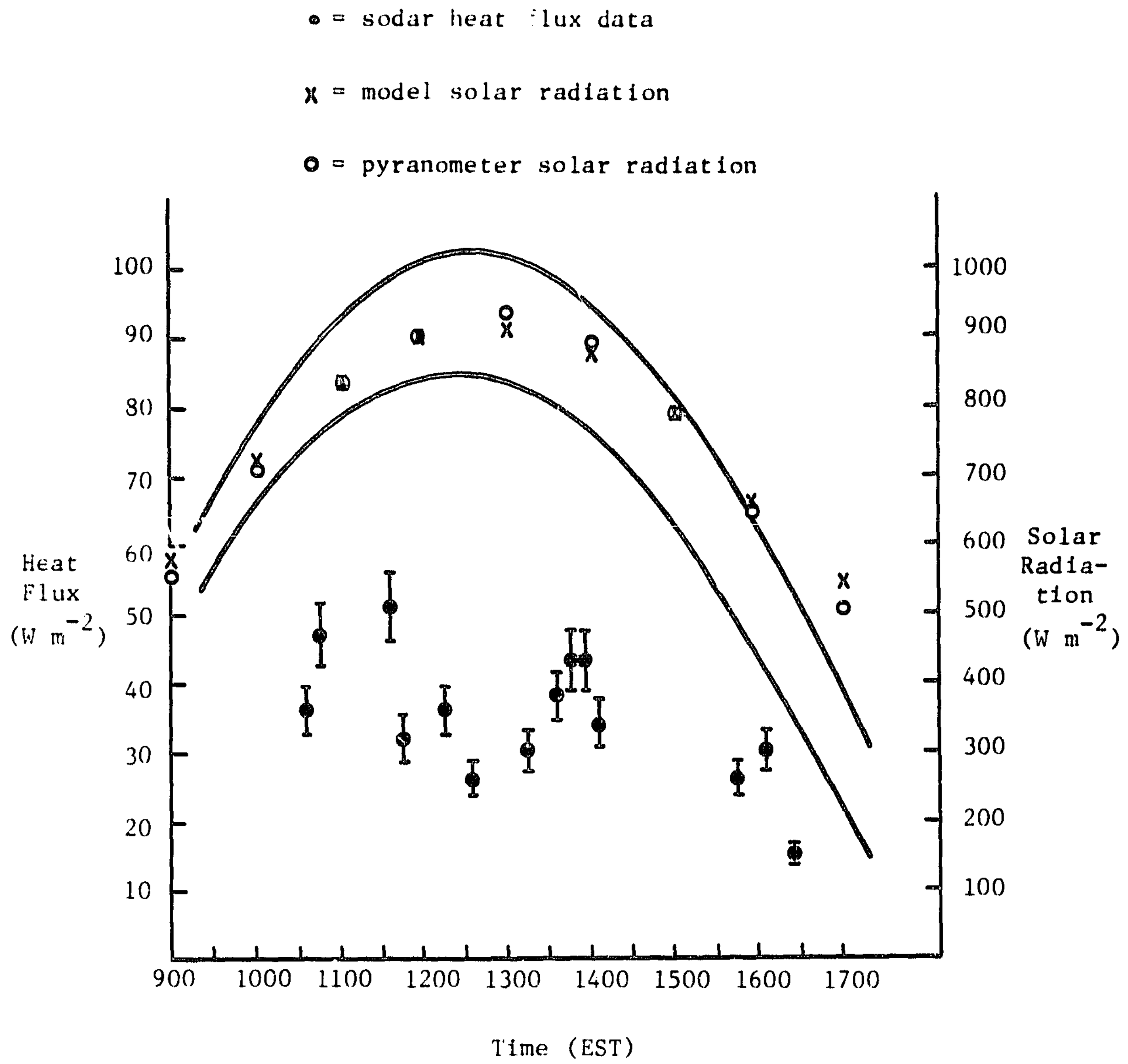

Figure 5.12 Heat flux and solar radiation data measured and calculated for Case 1.

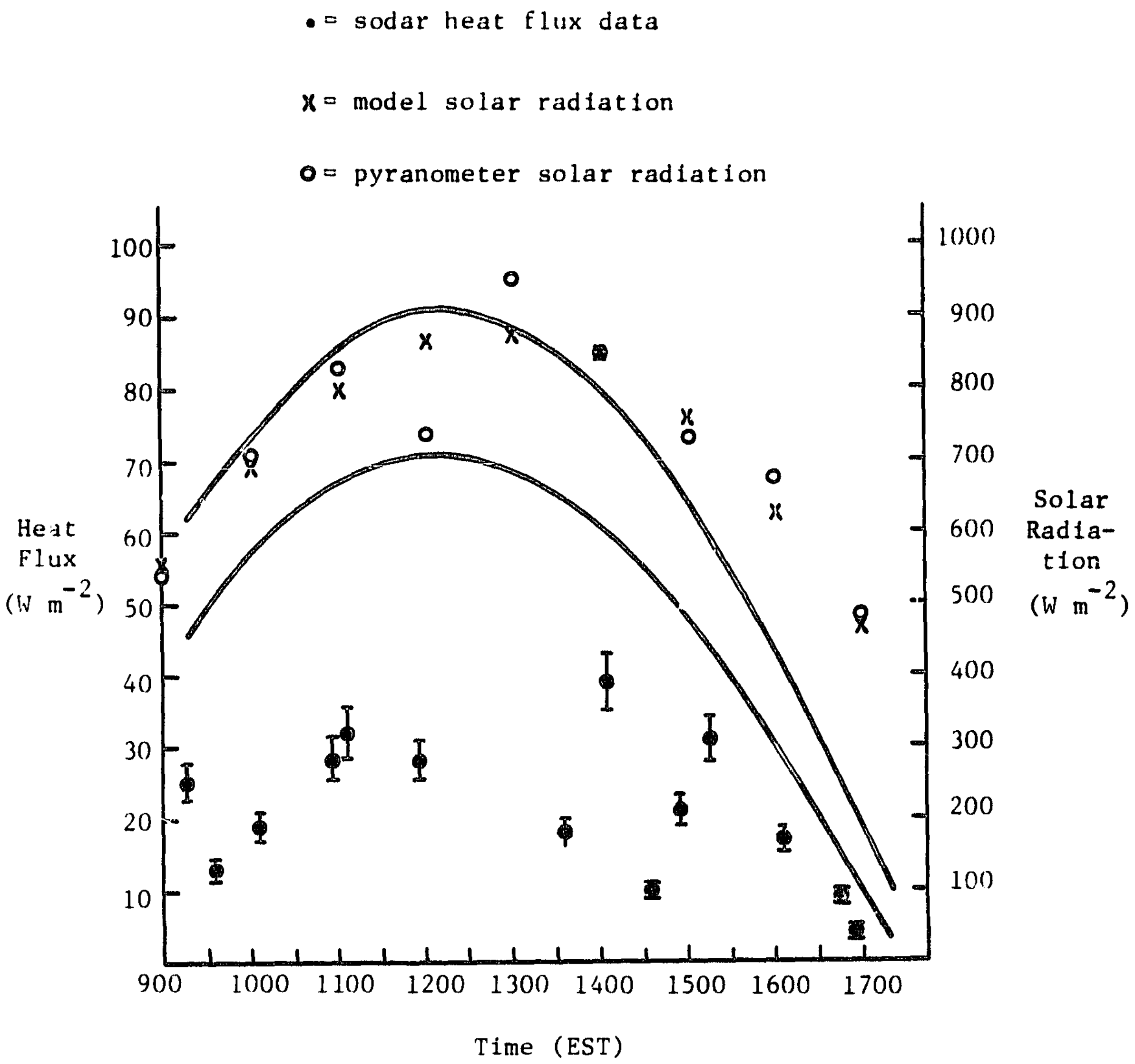

Figure 5.13 Heat flux and solar radiation data calculated and measured for Case 2.

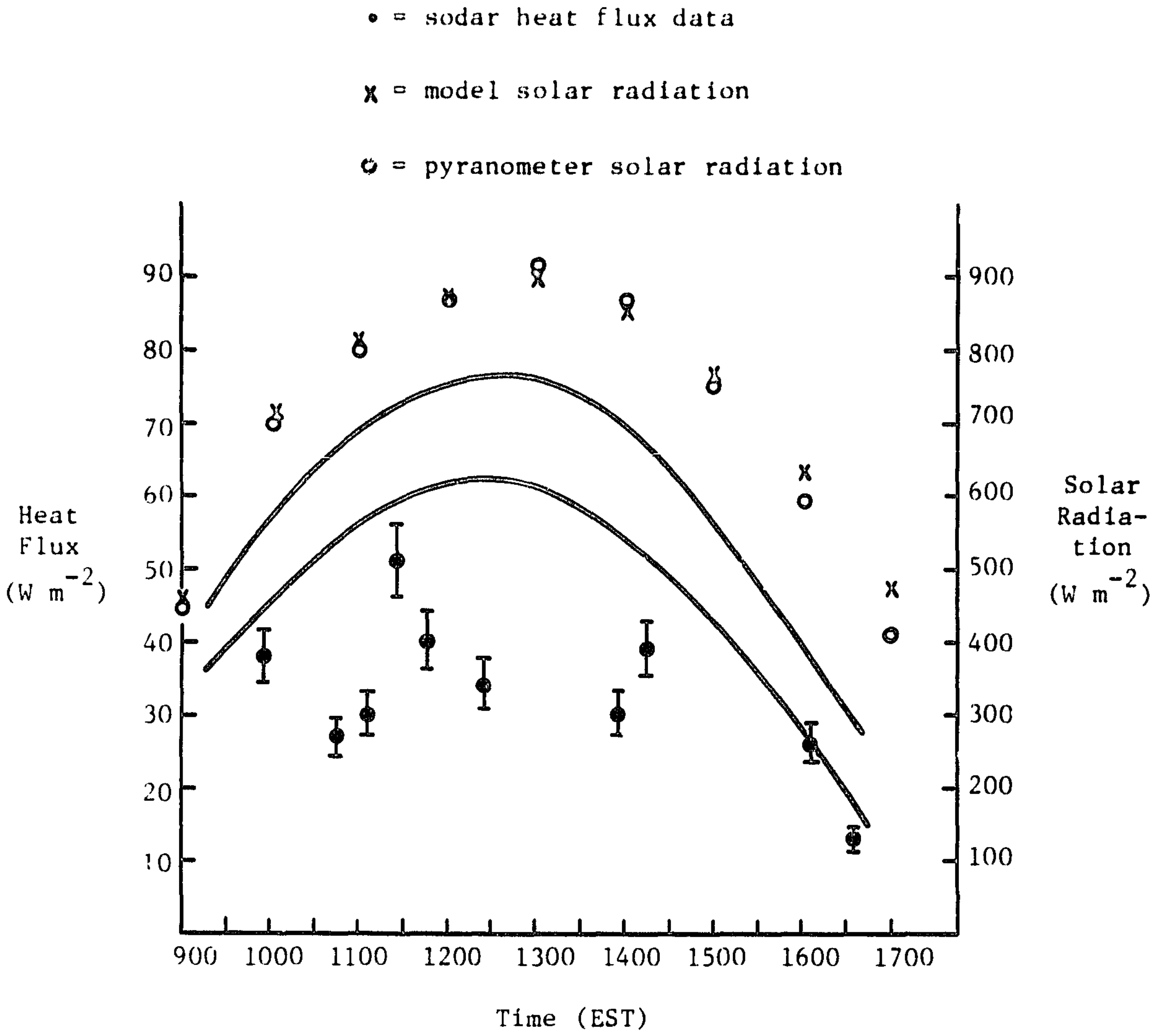

Figure 5.14 Heat flux and solar radiation data calculated and measured for Case 3.

1. Uncertainties in the calibration of the sodar.
2. Excess attenuation from turbulence of the sodar signal.
3. An increase in the sodar signal caused by humidity fluctuations.

The calibration process as described by Underwood (1978) requires a measurement of the acoustic pressure at the antenna beam axis and the variation of output acoustic power with RMS voltage given to the transducer. Both these measurements are determined in part using a microphone placed in the far field of the antenna beam pattern. If the microphone is not in the far field of the antenna, the sodar will be incorrectly calibrated. The far field of an antenna begins at about ten times the antenna diameter. Since the Aerovironment antenna is 1.2m in diameter, the microphone should have been at least 12m away. The calibration for this experiment was performed with the microphone approximately 7m from the antenna. Thomson (1981) estimated that the sodar heat fluxes could be in error from this problem by 5%.

Excess attenuation of the sodar signal is caused by turbulent spreading of the acoustic beam (Underwood, 1981a). The amount of excess attenuation is dependent on the antenna beam pattern and several atmospheric variables. Figure 5.15 developed by Underwood (1981c) was used to determine the excess attenuation term E in equation 2.1 for this experiment and was drawn using a friction velocity of 0.20 ms^{-1}, a frequency of 1600 hz, an antenna diameter of 1.2m, and an inversion height of 1000m. By determining the average z_i ($\sim$ 1000m), z/z_i (.15), and $z_i/-L$ (200) for the first three cases from the RDMS results, E was estimated from Figure 5.15 as 10%. Since this value is only an estimate of the average E and the heat flux varies as the .75

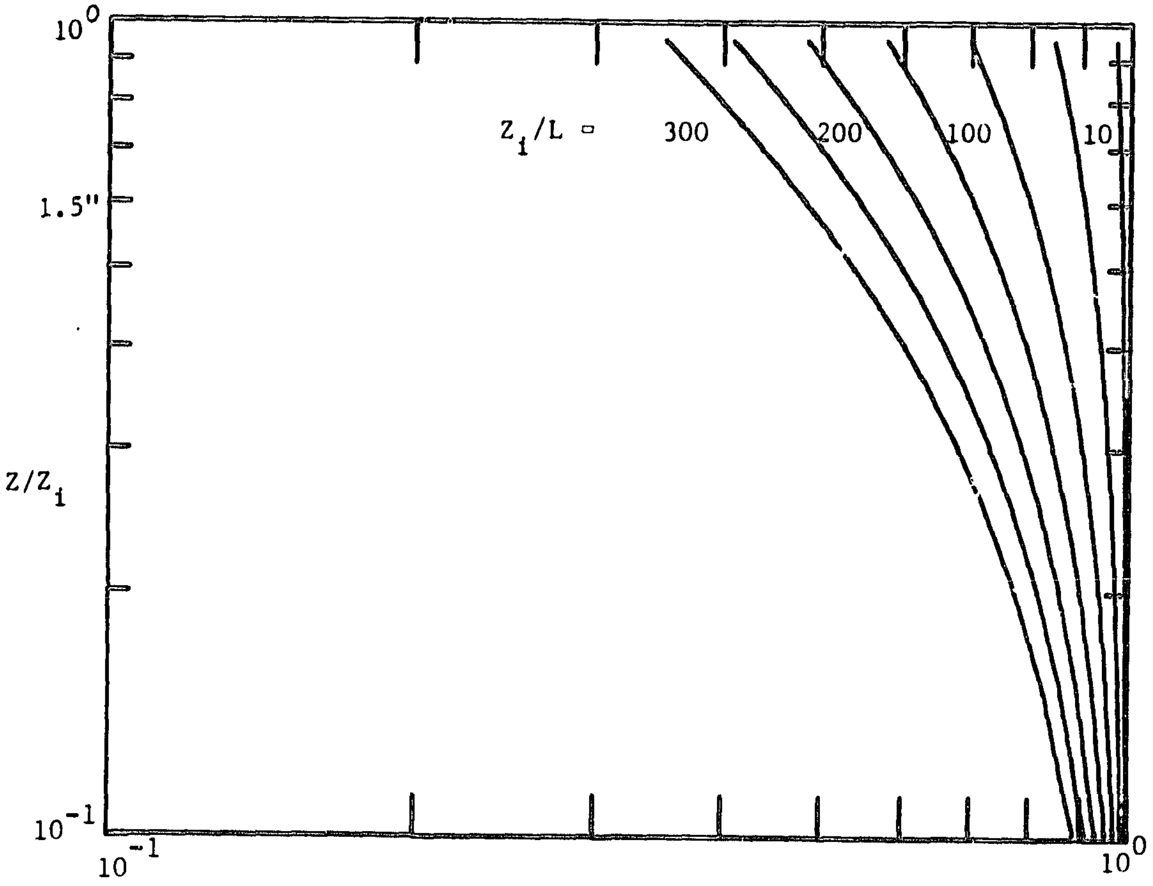

Excess Attenuation (E)

Figure 5.15 Plot of excess attenuation (E) versus Z/Z_i for various values of Z_i/L used to estimate the error in the sodar results caused by excess attenuation. (Source: Underwood (1981c)).

power of C_T^2, the reduction in the sodar heat flux values due to excess attenuation was established at 10%.

Humidity fluctuations can cause the sodar to overestimate the heat flux by increasing the amount of backscattered energy. Coulter and Wesely (1980) derived a correction factor γ_{so} that utilizes Bowen ratio measurements to correct sodar heat flux values for humidity fluctuations. To a first approximation, for all values of the Bowen ratio

$$\gamma_{so} \approx (1 + 0.07/\beta_s)^{-1} \tag{5.5}$$

where β_s is the surface Bowen ratio. Multiplying γ_{so} times the measured heat flux produces the correct value. Since no measurements of the evaporative flux were made in this experiment, an average RDMS value of the Bowen ratio in the first three cases was computed. Using this value for β_s in equation 5.5, γ_{so} was approximately 0.7.

The three aforementioned error sources were combined into a correction factor that lowered all the sodar-derived heat fluxes by 15%. The corrected values are plotted in Figures 5.12-5.14. The error bar on each value represents a 10% uncertainty following Coulter and Wesely (1980). The actual comparison of the RDMS and sodar heat flux values was disappointing. In Case 3, the magnitudes were somewhat smaller, but there was a severe lack of agreement ($\sim$ 30-50 W m^{-2}) in Cases 1 and 2.

The disagreement of Case 1 (Figure 5.12) was characterized by the sodar values being about 45 W m^{-2} lower than the RDMS heat fluxes between 1130 and 1330 EST. While the smooth RDMS heat flux curve was peaking, the sodar estimates suddenly dropped to a lower level. In the hours leading up to 1130 EST, the RDMS and sodar results disagreed in magnitude by 25 to 35 W m^{-2}, but increased at the same rate. At 1330 EST, the sodar estimates gained 5 to 10 W m^{-2}. Thereafter, the rate of decrease of the sodar heat fluxes matched that of the RDMS values. This afternoon period (1330-1700 EST) had better agreement than the morning period since the heat flux magnitudes differed by only 10 to 30 W m^{-2}.

The sodar results of Case 2 (Figure 5.13) followed the same basic pattern of Case 1. Between 900 and 1130 EST, the sodar values were 35 to 45 W m^{-2} too low, but increased at the same rate as the RDMS values. Between 1130 and 1500 EST, 4 out of the 5 sodar values were at a level 10 to 25 W m^{-2} below the values at 1105 and 1515 EST. The exception for this period was one sodar value at 1405 EST that was within 20 W m^{-2} of the RDMS estimate. After 1500 EST, the sodar results were within 15 W m^{-2} of the RDMS heat flux curve in magnitude and declined at the same rate.

Case 3 (Figure 5.14) also had the same pattern of midday disagreement, but the RDMS and sodar values of the afternoon and morning periods were much closer than in the first two cases. The morning period of 900 to 1200 EST had two values within 10 W m^{-2} of the RDMS results. Three values were only 15 to 30 W m^{-2} lower than the RDMS estimates and had the same rate of increase. Between 1200 and 1400 EST, only two sodar estimates were obtained. These sodar values were 20 to 30 W m^{-2} less than the RDMS values for that time and 10 to 15 W m^{-2}

below the sodar estimates at either end of the period. In the afternoon period for Case 3 (1415–1700 EST), the RDMS and sodar magnitudes were close. All the sodar values were within 10 W m^{-2} of the RDMS values.

Since an energy budget equation is the basis of the boundary layer model in the RDMS, if the model cannot accurately predict the amount of incoming solar radiation, the RDMS results will be invalid. Pyranometer data from the Penn State Weather Observatory were available for Cases 1-4 and 7. The model-predicted and measured solar radiation values are included in Figures 5.12–5.14. The agreement between the measured and predicted values is excellent. This result indicates that the RDMS heat flux curves are valid for Cases 1-3. The comparison for Case 7 is not as good, however (see Figure 5.16). The boundary layer model is overestimating the measured solar radiation by ∿ 500 W m^{-2} during the middle part of the day. In Case 7, therefore, the RDMS results may be incorrect since they are based on more solar radiation than was actually received.

In the preceding discussion, a pattern of agreement in the trend of the values for a morning and afternoon period emerges. During the midday hours a period of strong (25 to 45 W m^{-2}) disagreement was present. Within this pattern, only Case 3 had comparable sodar and RDMS magnitudes for the heat flux. The boundary layer model and pyranometer solar radiation data agreed almost exactly for Cases 1-3.

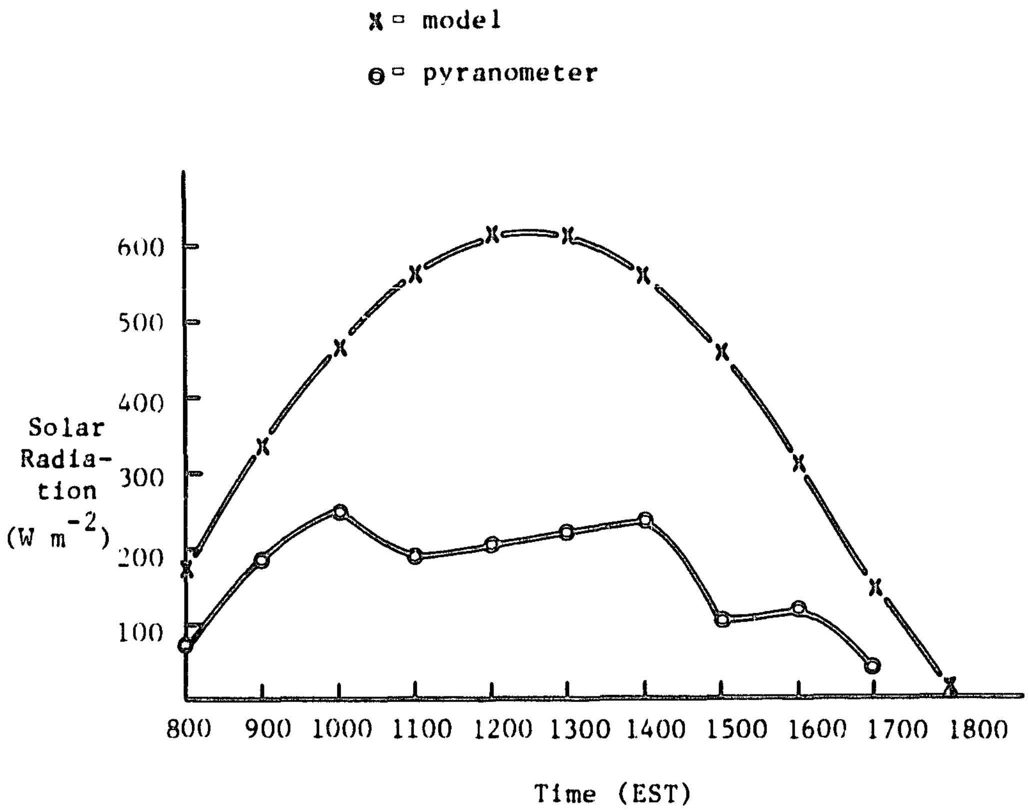

Figure 5.16 Pyranometer-measured and model-calculated solar radiation for Case 7.

6.0 CONCLUSIONS AND RECOMMENDATIONS

The purpose of this research was to validate a method that uses remotely derived surface temperatures and a boundary layer model to estimate surface energy budgets and certain surface parameters. Because remotely sensed temperature measurements tend to represent values averaged over an area, the surface fluxes determined using such data must also be area-averages. To carry out an effective validation study, ground truth data must be obtained from an independent technique which also produces area-averaged values.

One such method is sodar. The sodar can produce heat flux estimates averaged over the same scale as the remotely sensed temperature data. By measuring the scattering of sound in a volume by temperature fluctuations using sodar, one can compute values of a temperature structure constant, C_T^2. C_T^2 can in turn be related to the surface heat flux by a 4/3 power law when free convection conditions exist in the atmosphere.

In this research, the remotely sensed temperature data was obtained using a hand-held radiometer. A simultaneous collection of radiometric surface temperature and sodar data was made on seven occasions between mid-July and mid-October 1980.

The comparison between the radiometric data/model system (RDMS) and sodar derived heat fluxes proved disappointing. Free convection conditions were not present in Cases 4-7 and only intermittently in Cases 1-3. The sodar heat fluxes obtained in the first two cases were 25 to 45 W m^{-2} lower than the RDMS values. In the third case, the sodar and RDMS heat flux values were within 20 W m^{-2} of each other.

The RDMS is a relatively untested method. It is difficult to make strong conclusions concerning its validity since the RDMS and sodar results disagree. However, the evidence presented indicates that the sodar values could be in error by greater than the 10% figure given by Coulter and Wesely (1980). A possible source for the poor sodar results was the presence of a persistent low level inversion. This inversion was formed by a warm plume advected over the valley sodar site from an elevated heated plateau.

The results do suggest, however, that the true heat fluxes were not underestimated by the RDMS. Therefore, the Bowen ratios over well-watered vegetation are likely to be quite small. Computation of an Antecedent Precipitation Index (API) suggests a decrease in the soil moisture between July and September. This decrease is also present in the RDMS results.

Any future attempts to validate the remotely-sensed surface temperature and boundary layer model method should take heed of the difficulties encountered in this research. If the radiometric surface temperature data is to be used again, a less subjective method to determine an area-averaged temperature should be developed. Steps should also be taken to improve the quality of the sodar results by insuring that the effects of complex terrain are minimized. In addition, the technique successfully used by Coulter and Wesely (1980) to obtain sodar-derived heat fluxes should be emulated. Their procedure includes simultaneous heat flux measurements using the eddy correlation method and real time display of C_T^2 profiles to determine conclusively if free convection exists. Improving the sodar results and using better surface temperature data will enable stronger conclusions to be drawn about the validity of the remotely sensed surface temperature and boundary layer model method.

c - 2

REFERENCES

Augustine, J. A., 1978: A detailed analysis of urban ground temperature using high resolution satellite measurements. M.S. Thesis, Department of Meteorology, The Pennsylvania State University.

Barnes, W. L. and Price, J. C., 1980: Calibration of a satellite infrared radiometer. Appl. Opt., 19, 2153-2161.

Blad, B. L. and Rosenberg, N. J., 1976: Measurement of crop temperature by leaf thermocouple, infrared radiometry and remotely sensed thermal imagery. Agronomy J., 65, 341-347.

Carlson, T. N. and Boland, F. E., 1978: Analysis of urban-rural canopy using a surface heat flux/temperature model. J. Appl. Meteor., 17, 998-1013.

Carlson, T. N., Dodd, J. K., Benjamin, S. G., and Cooper, J. N., 1981: Satellite estimation of the surface energy balance, moisture availability and thermal inertia. J. Appl. Meteor., 20, 67-87.

Conway, J. and Van Bavel, C. H. M., 1967: Evaporation from a wet soil surface calculated from radiometrically determined surface temperatures. J. Appl. Meteor., 6, 650-655.

Coulter, R. L. and Wesely, M. L., 1980: Estimates of surface heat flux from sodar and laser scintillation measurements in the unstable boundary layer. J. Appl. Meteor., 19, 1209-1222.

DiCristofaro, D. C., 1980: Remote estimation of the surface characteristics and energy balance over an urban-rural area and the effects of surface heat flux on plume spread and concentration. M.S. Thesis, Department of Meteorology, The Pennsylvania State University.

Dodd, J. K., 1979: Determination of surface characteristics and energy budget over an urban-rural area using satellite data and a boundary layer model. M.S. Thesis, Department of Meteorology, The Pennsylvania State University.

Fuchs, M., Kanemasu, E. T., Kerr, J. P., and Tanner, C. B., 1967: Effect of viewing angle on canopy temperature measurements with infrared thermometers. Agronomy J., 59, 494-496.

Fuchs, M. and Tanner, C. B., 1966: Infrared thermometry of vegetation. Agronomy J., 58, 597-601.

Fuchs, M. and Tanner, C. B., 1968: Surface temperature measurements of bare soils. J. Appl. Meteor., 7, 303-305.

REFERENCES (Continued)

Heilman, J. L. and Kanemasu, E. T., 1976: An evaluation of a resistance form of the energy balance to estimate evapotranspiration. *Agronomy J.*, 68, 607-611.

Kocin, P. J., 1979: Remote estimation of surface moisture over a watershed. M.S. Thesis, Department of Meteorology, The Pennsylvania State University.

Lipschutz, R. A., 1978: An experimental study of the relationship of surface wind fluctuations to the stability, mixing depth and terrain. M.S. Thesis, Department of Meteorology, The Pennsylvania State University.

Neff, N. D., 1975: Quantitative evaluation of acoustic echoes from the planetary boundary layer. NOAA Technical Report ERL 322-WPL-38, NOAA, ERL, Boulder, CO, 34 pp.

Schiermeier, F. A., Wilson, W. E., Pouler, F., Ching, J. K., and Clarke, J. F., 1979: Sulfur transport and transportation in the environment (STATE): A major E.P.A. research program. *Bull. Amer. Meteor. Soc.*, 60, 1303-1312.

Sellers, W. D., 1965: *Physical Climatology*, The University of Chicago Press, Chicago, 272 pp.

Tatarski, V. I., 1971: The effects of the turbulent atmosphere on wave propagation. U.S. Department of Commerce, IPST Cat. No. 5319, NTIS, Sprinfield, Virginia.

Thomson, D. W., 1981: Error in [illegible] heat flux values from the calibration procedure. Private communication, June 1981.

Underwood, K. H., 1978: A quantitative study of cooling tower plumes using a monostatic sodar. M.S. Thesis, Department of Meteorology, The Pennsylvania State University.

Underwood, K. H., 1981a: Sodar signal processing for the Risø 78 Experiment. Ph.D. Thesis, Department of Meteorology, The Pennsylvania State University.

Underwood, K. H., 1981b: Presence of low level inversions in Rock Springs sodar data. Private communication, April 1981.

Underwood, K. H., 1981c: Calculation of the error in sodar heat flux values from excess attenuation. Private communication, May 1981.

Wyngaard, J. C., Izumi, Y., and Collins, S. A., Jr., 1971: Behavior of the refractive index structure parameter near the ground. *J. Opt. Soc. Amer.*, 61, 1646-1650.

APPENDIX A

SURFACE TEMPERATURE ERROR FROM ASSUMING A GROUND EMISSIVITY OF ONE

Many investigators (Fuchs and Tanner (1966), Conway and Van Bavel (1967), Fuchs and Tanner (1968)) using radiometers to determine vegetation and surface temperatures, estimated the surface emissivity and atmospheric downwelling radiation in order to increase the accuracy of their measurements. An investigation into the error caused by assuming a surface emissivity of one is shown below. From that explanation, it was determined that for the purposes of this research it was not necessary to take the reflected downwelling radiation into account.

Figure A.1 shows that the longwave radiation reaching the radiometer is a combination of ground and reflected downwelling radiation from the atmosphere. This situation can be written mathematically using Planck's Law as

$$\sigma\, T_e^4 = \varepsilon_g\, \sigma\, T_o^4 + (1-\varepsilon_g)\varepsilon_a\, \sigma\, T_a^4 \tag{A.1}$$

where

σ = Stefan Boltzman constant,

T_e = effective temperature as measured by the radiometer,

ε_g = emissivity of the ground,

T_o = actual ground temperature,

ε_a = emissivity of the air,

T_a = temperature of the air.

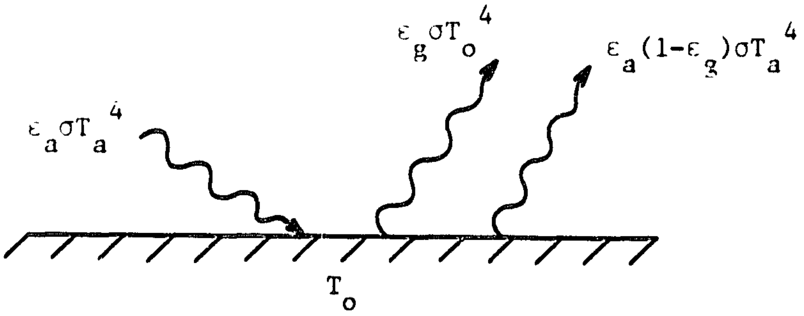

Figure A.1 Illustration of the longwave radiation reaching a radiometer.

ε_g = emissivity of the ground
ε_a = emissivity of the **air**
T_a = temperature of the air
T_o = temperature of the surface

Solving equation A.1 for the actual temperature T_o yields

$$T_o = \left[\frac{\sigma T_e^4 - (1-\varepsilon_g)\varepsilon_a \sigma T_a^4}{\varepsilon_g \sigma}\right]^{1/4} \qquad \text{(A.2)}$$

By using some reasonable values in (A.2), an estimate of the difference between the real and actual values for this research can be obtained. It if is assumed that

the effective temperature T_e is 300 K,

the air temperature T_a is 300 K,

the emissivity of the air e_a is 0.8 (Sellers (1967)),

and the emissivity of the ground ε_g is 0.98 (Fuchs and Tanner (1966)),

then the actual ground temperature T_o is 300.31 K. Thus, the actual temperature is only .3C warmer than the temperature measured by the radiometer. It is clear then, that to achieve an accuracy of ± 0.1C, one must determine the actual emissivity of the ground.

However, two other error sources in this experiment overwhelm the emissivity error.

1. Tanner et al. (1967) noted a ± 0.3C variation in time with their temperature measurements just from air turbulence.
2. A pre-experiment calibration of the radiometer showed that it consistently overestimated the temperature of a stirred water surface by 1.5 to 2C. This error was accommodated by subtracting a constant 1.7C from the measurements.

The additional effort of determining the surface emissivity of the heterogeneous cropland at the Rock Springs site is clearly not worth the effort. The error from assuming a surface emissivity of one is lost in the radiometer and turbulence errors which combined, make each measurement accurate to ± 0.5C. Since satellite radiometric and the boundary layer model temperatures are accurate only to ± 1 or 2C, the error of ± 0.5C is acceptable.

APPENDIX B

SURFACE TEMPERATURE MEASUREMENTS FROM AN AIRBORNE RADIOMETER

In Case 6, in addition to the regular surface temperature measurements, temperature data were collected from an airborne radiometer. An Everest Infrared Thermometer with a 3 degree field of view was flown four times at about 150m over the Rock Springs site. During the overflights, temperature values for various crops were recorded. The raw data are presented in Table B.1. The Everest radiometer does not assume an emissivity of one in producing its temperature values. Unlike the Barnes radiometer used on the ground, the Everest user specifies an emissivity from 0 to .99. Thus, the theory discussed in Appendix A must be altered to include the radiometer radiometer emissivity ε_r. Putting ε_r in equation A.1 we obtain

$$\varepsilon_r \sigma T_e^4 = \varepsilon_g \sigma T_o^4 + \varepsilon_a \sigma T_a^4(1-\varepsilon_g) \quad . \tag{B.1}$$

We want to calculate how much the radiometer-measured (effective) temperature T_e changes when ε_r is changed from a value of one. If we assume ε_g is constant and known and differentiate (B.1) with respect to ε_r we get

$$\varepsilon_r 4T_e^3 \frac{\partial T_e}{\partial \varepsilon_r} + T_e^4 \varepsilon_r = 0 \tag{B.2}$$

Solving (B.2) for $\frac{\partial T_e}{\partial \varepsilon_r}$, the result is

Table B.1 Case 6 surface temperature data from an airborne hand-held radiometer.

Pass 1		Pass 2		Pass 3		Pass 4	
T(°C)	Crop	T(°C)	Crop	T(°C)	Crop	T(°C)	Crop
24.6	Corn	26.4	Grass	23.0	Corn	23.6	Corn
27.0	Corn	25.6	Grass	25.6	Corn	24.6	Corn
21.8	Corn, Grass	26.4	Grass	26.0	Grass	23.8	Corn
22.2	Corn	22.1	Corn				
23.0	Corn	24.2	Grass				
25.4	Corn	23.6	Corn				
		23.3	Corn				
		24.2	Corn				

$$\frac{\partial T_e}{\partial \varepsilon_r} = -\frac{T_e}{4} \qquad (B.3)$$

Using finite differences, we can solve for the change in T_e caused by a change in ε_r from a value of one.

$$\Delta T_e = \left(\frac{T_e}{4}\right) \Delta\varepsilon_r \qquad (B.4)$$

To compare the Everest temperature measurements with the temperatures made on the ground, a correction in the Everest T_e for an ε_r of .98 must be made following the theory previously discussed. If the Everest measures a temperature of 300 K using an ε_r of .98, $\Delta\varepsilon_r$ is -0.02 and the corrected Everest temperature is 1.5 K warmer than the measured value.

The average Everest temperature for the site was 24.3C. Adding in the correction factor of 1.5C, the result is 25.8C. This value is 1.5C cooler than the 27.3C estimated from the ground data. However, the uncertainty of the ground estimate is ± 2.5C and no water vapor correction was made to the Everest value. The biggest difference between the two sets of temperatures was the spread in the values. The ground data went from 21.1C to 29.6C while the Everest values ranged from 23.6C to 28.5C. The Everest values narrow down, but do not extend beyond the range of ground values. The agreement between the estimated area-averaged values indicates that the subjective analysis performed on the ground temperature data produces a reasonable area-averaged temperature value.

APPENDIX C

DETERMINATION OF RDMS HEAT FLUX FOR CASE 3

The boundary layer model, after having been suitably initialized for Case 3 (July 25, 1980), was run for the period 0600 to 2400 EST 16 times using different moisture availability (M) and thermal inertia (P) combinations that spanned those parameters likely ranges (M = 0.25-1, P = 0.005-0.08). The surface temperature data for Case 3 was collected at 1500 EST and 2400 EST. At those times, the model output for each M and P combination was extracted and stored. As a simple way of representing the 16 sets of model output, second order regression equations were formed with surface temperatures as predictors and M, P, or a surface flux as the predictand. The regression equations had the form

$$X = C_0 + C_1T_d + C_2T_d^2 + C_3T_N^2 + C_4T_N^2$$

where X is M, P, heat flux, etc., C_0-C_5 are the regression coefficients for the parameter, T_d is the day surface temperature, and T_N is the night surface temperature. In this research, the important equations were those predicting M and P and the regression coefficients for those equations are given in Table C.1.

The next step was to use the observed surface temperatures to predict an M and P value for this case. T_d and T_N, estimated at 30.3C and 14.3C, respectively, produced an M of 1.0 and a P of 0.068. To determine the RDMS heat flux estimate for Case 3, the model was run again with the same set of initial conditions, but M and P were held fixed at 1.0 and 0.068, respectively. The resulting diurnal heat flux curve and its uncertainty are plotted as a swath in Figure 5.14.

Table C.1 Regression coefficients for M and P in Case 3.

	M	P
C_0	4.75	0.446
C_1	-0.165	-0.0201
C_2	0.0376	-0.00504
C_3	0.00147	0.00231
C_4	-0.00289	0.000451